Structural Optimization of a Distributed Actuation System in a Flexible In-plane Morphing Wing

THESIS

James T. Westfall, Captain, USAF

AFIT/GAE/ENY/07-J22

DEPARTMENT OF THE AIR FORCE
AIR UNIVERSITY

AIR FORCE INSTITUTE OF TECHNOLOGY

Wright-Patterson Air Force Base, Ohio

APPROVED FOR PUBLIC RELEASE; DISTRIBUTION UNLIMITED.

The views expressed in this thesis are those of the author and do not reflect the official policy or position of the United States Air Force, Department of Defense, or the United States Government.

AFIT/GAE/ENY/07-J22

Structural Optimization of a Distributed Actuation System in a Flexible In-plane Morphing Wing

THESIS

Presented to the Faculty

Department of Aeronautics and Astronautics

Graduate School of Engineering and Management

Air Force Institute of Technology

Air University

Air Education and Training Command

In Partial Fulfillment of the Requirements for the

Degree of Master of Science in Aeronautical Engineering

James T. Westfall, B.S.M.E.

Captain, USAF

June 2007

APPROVED FOR PUBLIC RELEASE; DISTRIBUTION UNLIMITED.

AFIT/GAE/ENY/07-J22

Structural Optimization of a Distributed Actuation System in a Flexible In-plane Morphing Wing

James T. Westfall, B.S.M.E.
Captain, USAF

Approved:

/signed/	11 Jun 2007
Dr. Robert Canfield (Chairman)	date
/signed/	11 Jun 2007
Dr. Brian Sanders (Member)	date
/signed/	11 Jun 2007
Dr. Donald Kunz (Member)	date

Abstract

Structural weight and efficiency are two major hurdles for morphing aircraft being realizable on the full-scale level, both of which are addressed in this research. The optimal distribution and orientation of actuators throughout an in-plane flexible morphing wing structure is investigated. The drive to minimize structural weight causes a wing to be more flexible and the location and orientation of the actuators become more critical as the structure becomes more flexible. NextGen's N-MAS morphing wing is used as a case study. The wing is modeled as a number of unit cells assembled in a scissor-like structure, each comprised of four linkages pinned together and an actuator. The flexible skin of the wing is modeled with a nonlinear material stretched between two opposing vertices. It will be shown that the optimal orientation of the actuators will vary depending on the loading conditions and initial configuration of the wing. Sequential quadratic programming (SQP) optimization techniques are utilized to orient those actuators and effectively size the members of the structure. The goal is to minimize weight while maximizing the geometric advantage and efficiency. The constraints are member stresses and the force transferred to the actuators is not to be greater than the force the actuator is able to produce. `Matlab`® code is developed to do the SQP optimization while NASTRAN™ is utilized to do the nonlinear finite element analysis required to evaluate the objective function and constraints. The single-cell results are compared to experimental data to validate the finite element model (FEM) and optimization routine. A three-cell experiment is designed by utilizing aeroelastic scaling techniques. `Matlab`® is used to develop the scaling problem while the actual scaling is done as an optimization in NASTRAN™. The objective for scaling the wing is to minimize the differences in the non-dimensional displacements and strain energies between the two models, using the element cross-sectional dimensions as design variables.

Acknowledgements

First and foremost, I would like to acknowledge my advisor, Dr. Canfield, for his direction and leadership throughout this research. I would also like to thank Drs. Sanders and Joo for sponsoring this research. Without their vision and direction, this work would not have been possible. I would also like to thank NextGen Aeronautics for all of the information and help they provided. Finally, I would like to thank Brian Smyers for his help in building and testing the experimental work.

James T. Westfall

Table of Contents

Page

Abstract iv

Acknowledgements v

List of Figures viii

List of Tables x

List of Symbols xii

List of Abbreviations xv

I. Introduction 1
- 1.1 Background 1
- 1.2 Problem Statement 4
  - 1.2.1 Geometry 5
  - 1.2.2 Metrics 6
  - 1.2.3 Optimization Problem 8
- 1.3 Overview 10
- 1.4 Implications 11

II. Literature Review 13
- 2.1 Adaptive Structures in Space 13
- 2.2 Adaptive Structures in Aircraft 15
- 2.3 Optimization Efforts 19

III. Methodology 21
- 3.1 Analytical Analysis 21
  - 3.1.1 Finite Element Analysis 21
  - 3.1.2 Optimization Routine 25
- 3.2 Experimental Validation 28
  - 3.2.1 Single-Cell Experiment 28
  - 3.2.2 Three-cell Experiment 34

IV. Results 44
- 4.1 Single-cell Experiment 44
- 4.2 Comparison of FEM and Experiment 54
- 4.3 Optimizations 58
- 4.4 Three-Cell Experiment Scaling 62

Page

V. Conclusions and Recommendations 65
5.1 Overview 65
5.2 Conclusions 66
5.3 Significance of Research 66
5.4 Recommendations 67

Appendix A. DMAP Code 69
A.1 DMAP Stiffness Output 69

Appendix B. Experimental Data 70
B.1 First Run 70
B.2 Second Run 75
B.3 Third Run 77
B.4 Fourth Run 79
B.5 Fifth Run 84
B.6 Sith Run 86
B.7 Seventh Run 88

Bibliography 90

Vita 93

Index Index-1

List of Figures

Figure		Page
1.1.	Spider plot comparison.	2
1.2.	N-MAS model.	3
1.3.	N-MAS morphing configuration.	4
1.4.	N-MAS substructure.	4
1.5.	Cell breakout.	5
1.6.	Three cell configuration.	6
2.1.	Puffer fish can morph.	14
2.2.	Bald eagle is able morph.	14
2.3.	DARPA "smart wing".	16
2.4.	MXF-1 remotely piloted morphing aircraft.	17
2.5.	MXF-1 topview morphed configurations.	18
3.1.	Single-cell finite element model.	22
3.2.	Flexible skin for N-MAS wind tunnel model.	22
3.3.	Stress-Strain curve for EL 80M.	23
3.4.	Single-cell experiment structure.	30
3.5.	Joint design for single-cell experiment.	31
3.6.	Single-cell experiment setup.	32
3.7.	Actuator and spring calibration.	35
3.8.	N-MAS finite element models.	38
3.9.	Aerodynamic models for N-MAS.	39
3.10.	Closeup of N-MAS finite element model.	40
3.11.	Distributed load used to scale three-cell experiment.	41
4.1.	Displacement measurement locations for single-cell.	45
4.2.	Repeatability test for X-displacement.	46
4.3.	Repeatability test for Y-displacement.	46

Figure Page

4.4. Repeatability test for actuator displacement. 47

4.5. Average efficiency for single-cell experiment runs. 47

4.6. Measured actuator force over three runs. 48

4.7. Spring force measurements. 49

4.8. Spring stiffness curve. 51

4.9. Spring material stress-strain curve. 53

4.10. Comparison of FEM and analytical x-displacement. 54

4.11. Comparison of FEM and analytical y-displacement. 55

4.12. Comparison of FEM and analytical actuator displacement. . . . 55

4.13. Comparison of FEM and analytical objective. 56

4.14. Exploring efficiency definition. 57

4.15. Analytical FEA results for parametrically varying design variable. 59

4.16. Design of three-cell scaled experiment. 63

List of Tables

Table		Page
3.1.	Final design specifications of single-cell experiment.	31
4.1.	Actuator Calibration Data.	48
4.2.	Mean force-displacement data.	50
4.3.	Spring stiffness data for single-cell experiment.	50
4.4.	Mean Stress-Strain Data.	52
4.5.	Optimization configurations.	58
4.6.	Single design variable optimization results.	60
4.7.	Multi-Objective optimization results.	61
4.8.	Final design efficiencies for multi-configuration optimization.	61
4.9.	Final design dimensions of the three-cell experiment.	64
B.1.	Experimental data for run 1, load case 1	70
B.2.	Experimental data for run 1, load case 2	71
B.3.	Experimental data for run 1, load case 3	71
B.4.	Experimental data for run 1, load case 4	72
B.5.	Experimental data for run 1, load case 5	72
B.6.	Experimental data for run 1, load case 6	73
B.7.	Experimental data for run 1, load case 7	73
B.8.	Experimental data for run 1, load case 8	74
B.9.	Experimental data for run 1, load case 9	74
B.10.	Experimental data for run 2, load case 1	75
B.11.	Experimental data for run 2, load case 2	76
B.12.	Experimental data for run 2, load case 3	76
B.13.	Experimental data for run 3, load case 1	77
B.14.	Experimental data for run 3, load case 2	78
B.15.	Experimental data for run 3, load case 3	78

Table Page

B.16. Experimental data for run 4, load case 1 79
B.17. Experimental data for run 4, load case 2 80
B.18. Experimental data for run 4, load case 3 80
B.19. Experimental data for run 4, load case 4 81
B.20. Experimental data for run 4, load case 5 81
B.21. Experimental data for run 4, load case 6 82
B.22. Experimental data for run 4, load case 7 82
B.23. Experimental data for run 4, load case 8 83
B.24. Experimental data for run 4, load case 9 83
B.25. Experimental data for run 5, load case 1 84
B.26. Experimental data for run 5, load case 2 85
B.27. Experimental data for run 5, load case 3 85
B.28. Experimental data for run 6, load case 1 86
B.29. Experimental data for run 6, load case 2 87
B.30. Experimental data for run 6, load case 3 87
B.31. Experimental data for run 7, load case 1 88
B.32. Experimental data for run 7, load case 2 89
B.33. Experimental data for run 7, load case 3 89

List of Symbols

Symbol		Page
L	Lift	3
D	Drag	3
ρ_{air}	Local air density	3
v^2	Aircraft speed	3
S	Wing planform area	3
C_L	Coefficient of lift	3
C_D	Coefficient of drag	3
$\vec{Z}_1$	Actuator mount location along spar	5
$\vec{Z}_2$	Actuator mount location along rib	5
$\vec{Z}_3$	Actuator vector	5
θ	Interior half angle of cell	5
d	Link length	5
F_{exy}	External force in y-direction	5
F_{exx}	External force in the x-direction	5
W_{struct}	Weight of the structure	7
ρ	Density of link	7
h	Height of link	7
w	Width of the link	7
n	Number of linkages in problem	7
i	Denotes individual link	7
W_{out}	Work out	7
X_{out}	Displacement in x-direction where F_{exx} is applied	7
Y_{out}	Displacement in y-direction where F_{exy} is applied	7
W_{in}	Work in	7
F_{act}	Force of the actuator	7

Symbol		Page
Δl_{act}	Change in actuator length	7
η	System efficiency	7
B	Blocking force	8
φ	Angle between actuator and x-axis	8
r	Objective weighting factors	8
N_g	Number of configuration	9
c_g	The weighting factor for each configuration efficiency	9
η_g	Efficiency for individual configuration	9
p	Actuator power factor	9
σ_i	Stresses of individual links	9
$\sigma_{\max}$	Maximum allowable stress	9
N_{act}	Number of actuators in system	9
N_{cells}	Number of cells	9
$w_{\min}$	Minimum link width allowed	10
K	Stiffness matrix	26
u	Displacements	26
P	Applied nodal forces	26
R	Residual	27
Δu	Step size	27
E	Modulus of elasticity	36
I_z	Area Moment of inertia	36
L_e	Length of element	36
V	Vertical displacement at given node	36
θ_{z1}	Rotation about z-axis at each node	36
F_v	Vertical force at each node	36
M	Moment at each node	36
L_o	Characteristic length	36
F_0	Characteristic force	36

Symbol		Page
A_0	Characteristic cross-sectional area of element	37
S_{wet}	Aircraft wetted surface area	39
S_{exposed}	Wing exposed planform area	39
(t/c)	Ratio of wing thickness to chord	39
$\overline{D}_L$	Nondimensional displacements for the large scale model	42
$\overline{D}_S$	Nondimensional displacements for the small scale model	42
$\overline{U}_L$	Nondimensional strain energies for the large scale model	42
$\overline{U}_S$	Nondimensional strain energies for the small scale model	42
N_e	Number of elements	42
N_n	Number of nodes	42
e	Denotes individual element number	42
n	Denotes individual node number	42
k_r	Stiffness constant of axial rod element	51
A_e	Cross-sectional area of element	51
ε	Strain	52
Δl_{spring}	Change in spring length	52

List of Abbreviations

Abbreviation		Page
N-MAS	NextGen Morphing Aircraft Structure	3
dof	Degree-of-freedom	4
COTS	commercial off the shelf	7
GA	geometric advantage	7
SQP	sequential quadratic programming	10
FEA	finite element analysis	10
FEM	Finite element model	10
UAV	unmanned aerial vehicle	11
MAW	Mission adaptive wing	15
AFW	Active flexible wing	15
DARPA	Defense Advance Research Projects Agency	16
SMA	Shape memory alloy	16
SMP	Shape memory polymers	17
DMC	Dynamic modulus composites	17
DMF	Dynamic modulus foam	17
MXF-1	Morphing flight-vehicle experiment	18
SQP	Sequential quadratic programming	25
DMAP	Direct Matrix Abstraction Program	43

Structural Optimization of a Distributed Actuation System in a Flexible In-plane Morphing Wing

I. Introduction

1.1 Background

The morphing wing concept traces its roots back to the first aircraft flown. The Wright brothers used wing warping as a way to provide stability and control. The wings on the this first aircraft were very flexible and easily warped using cables and pulleys. Throughout time aircraft have gotten larger, and carry more loads. This has driven the wings of modern day aircraft to be much more rigid than the Wright brothers' first aircraft. The more rigid wings of modern aircraft are not as easily warped, but advances in materials, actuation systems, and mechanization have made shape changing of modern wings feasible.

The Wright brothers used the morphing wing concept for stability and control purposes, and the morphing concept is being researched for the same reason today, as well as a few others. One area that morphing wings can improve is aircraft performance. Modern aircraft are designed for a particular mission. The F-16 was designed to be a cheap, maneuverable, fighter aircraft. It is excellent at high speed maneuvering, but not good at loitering over a target and collecting information. The Predator on the other hand is designed just for that, but it is not good at high speed maneuvering. The difficulty is that each aircraft is doing more than the mission that it is designed for. The F-15 is a great example of this. It is a multi-role aircraft, that is designed primarily to be good at high speed maneuvering and supersonic flight. The F-15, as with many aircraft, still has to climb out, cruise to way points, loiter about a targeted region, and perform its designed mission of high speed maneuvering

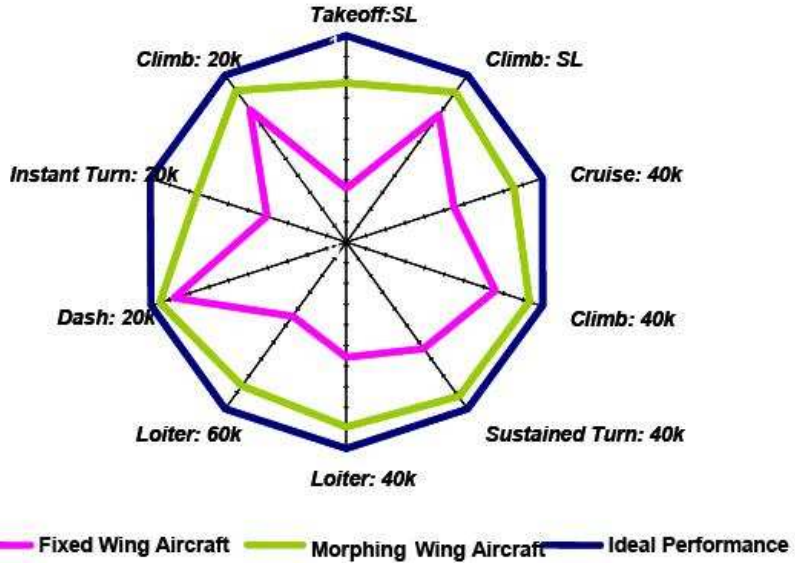

Figure 1.1: Spider Plot comparing a fixed wing to a morphing wing [6].

to deliver munitions and maintain air superiority. While this aircraft does extremely well during one leg in its designed mission, it also suffers efficiency losses during the other legs of the mission. The concept of morphing aircraft is to be able to change the shape of the aircraft in a way that will allow it to better perform during all of the needed legs of a mission. Figure 1.1 shows a typical fixed wing aircraft as compared to a conceptual morphing wing aircraft. The outside line is plotted for the ideal design for each mission performed. It is obvious that the fixed wing aircraft is good at at a few design points such as dash, but is lacking in others such as takeoff. A morphing aircraft can be designed to have better performance at each of the design points, and thus making it a closer match to the ideal case for each of the mission legs.

One way to be able to control the performance of an aircraft at different design points is to be able to control the lift and drag of the aircraft.

$$L = \frac{1}{2}\rho_{air} v^2 S C_L \tag{1.1}$$

$$D = \frac{1}{2}\rho_{air} v^2 S C_D \tag{1.2}$$

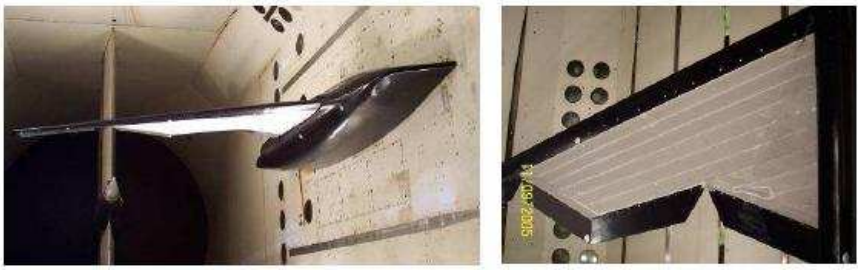

Figure 1.2: Front and top views of N-MAS model in the NASA LaRC transonic wind tunnel [13].

Where L is the lift, D is the drag, ρ_{air} is the local air density, v^2 is the aircraft speed, S, is the wing planform area, C_L is the coefficient of lift, and C_D is the coefficient of drag. Equations (1.1) and (1.2) show that both lift and drag are determined in part by the wing planform area. Changing the area of the wing is one way to control the performance of an aircraft, and current morphing wing designs can change the are by as much as 100% [28]. The performance of an aircraft can also be controlled by changing both the coefficients of lift and drag. This can be done by means of a change in camber, sweep angle, chord, and/or span. The focus of this research was based on an aircraft that can change the sweep angle, span, chord, and planform area.

The aircraft used for this research was design by NextGen Aeronautics, Inc., of Torrance California. The NextGen Morphing Aircraft Structure (N-MAS) is a 2400-lb vehicle that can undergo a 200% change in aspect ratio, 40% in span and 70% in wing area [2, 6]. The half-span wind tunnel model shown in Fig. 1.2 is a 1200 lb model that can change area from 15 to 24 sq-ft, sweep angle from 15 to 45 degrees, and half-span from 7 to 10 ft. Wind tunnel testing of the model proved that it was capable of morphing under aerodynamic loading. The model was tested at mach numbers "varying from 0.2 to 0.9 and operating conditions representative of altitudes varying from sea level to 50,000 ft [6]." There were five distinct configurations that the N-MAS aircraft model was able to change shape into and those can be seen in Fig. 1.3. These different configurations are achieved by an underlying adaptive structure wrapped in an elastic skin, that is able carry out-of-plane loads of up to 400 psf. The adaptive substructure, shown in Fig. 1.4, is a two degree-of-freedom

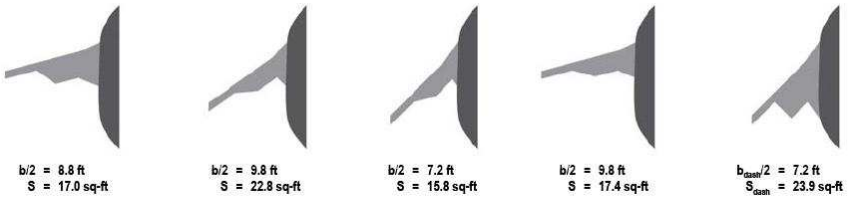

Figure 1.3: Morphing wing configurations for each of the design points [6].

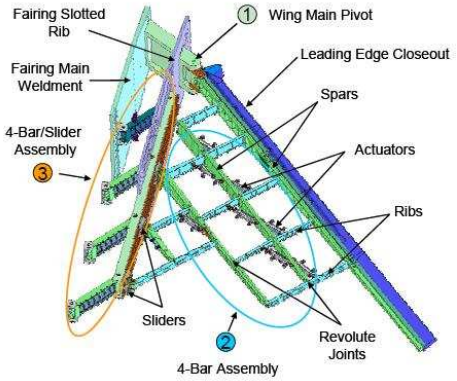

Figure 1.4: Morphing wing substructure [2].

(dof) system. The system configuration can be described by the sweep angle and the internal angle on the trailing edge 4-bar linkage. There are nine actuators located in the N-MAS half-span model substructure. Eight actuators are in the main wing 4-bar assembly, shown in section two of Fig. 1.4, and the other actuator is not shown, but is located in the root 4-bar/slider assembly, section three. The focus of this research work was to determine where the actuators should be located and how they should be orientated, so that the system achieves maximum efficiency.

1.2 Problem Statement

Current morphing wing designs are too heavy and require too much power to be feasible at the full-scale level. The goal of this research is to develop a process to minimize the structural weight and at the same time maximize the efficiency of the distributed actuation system. The distributed actuation system influences the overall structural weight and efficiency and studying its effects for one test case will

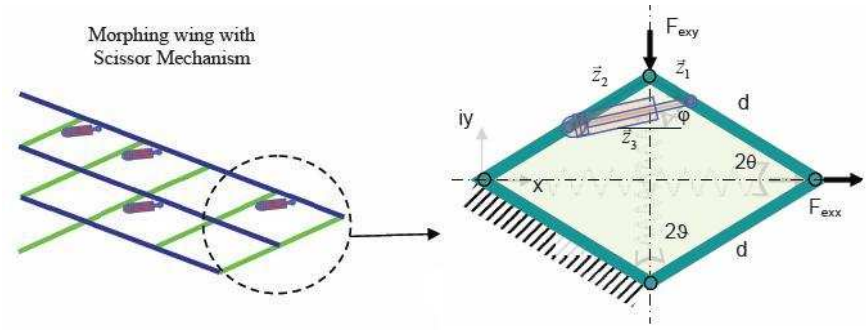

Figure 1.5: Simplified schematic of scissor-like morphing substructure with a cell breakout, including actuator and external load [18].

provide insight into its influence in general so that results can be used to shape the design process for various types of morphing aircraft. Eventually weight and efficiency optimization will contribute to morphing aircraft being feasible on the full-scale level. The developed optimization process will be validated using experimental results. The N-MAS wing design will be used as a test case throughout the research. The adaptive substructure that allows the N-MAS wing to morph was first simplified so that some basic parameters could be defined. These parameters were then used to define the efficiency. Determining the location and orientation of the actuators was then done using a multi-objective structural optimization approach.

1.2.1 Geometry. The N-MAS wing can be described as a system of cells, and the cell can be defined as in Fig. 1.5, where $\vec{Z}_1$ is the vector along the spar where the actuator is mounted, $\vec{Z}_2$ is the vector along the rib where the actuator is mounted, $\vec{Z}_3$ is the vector representing the actuator location, θ is the interior half angle used to describe the cell configuration, d is the length of the link, F_{exy} is the external force in the y-direction, and F_{exx} is the external force in the x-direction. The stiffness of the skin was modeled as a spring mounted between two opposing vertices. Only a spring in tension was needed, as skin pre-strain was not modeled.

Multiple single cells can then be put together to create different configurations. One that was looked at in this research was the three-cell model shown in Fig. 1.6. In

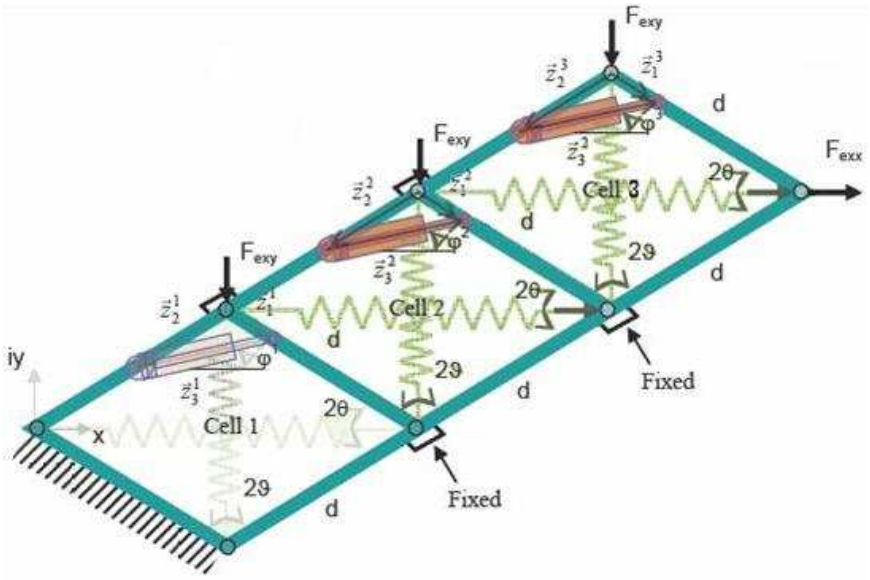

Figure 1.6: Three cell configuration, showing two active actuators [18].

multiple-cell configurations, there are typically fewer actuators than cells. Actuator location refers to which cells should have actuators, where as actuator orientation refers to how the actuators should be mounted in those cells.

1.2.2 Metrics. Using the system parameters described, various different metrics were defined, so that they could be used to evaluate the overall desirability of the design. As with all aircraft design, one of the goals is always to reduce the weight to a minimum. Therefore, one of the metrics is overall weight of the system. The number and size of actuators was predetermined and constant for all problems, so the change in weight only came from the change in cross-sectional areas of the spars and ribs. The N-MAS aircraft utilizes complex tapered C-channels and I-beams, but for simplification purposes, this research assumed all links in the scaled-down models have a uniform rectangular cross-section. The weight was then defined as

$$W_{struct} = \sum_{i=1}^{n} \rho_i h w_i d_i \tag{1.3}$$

where W_{struct} is the wight of the structure, ρ is the mass density of the link, h is the height of the link (held constant throughout structure), w is the width of the link, n is the number of linkages in the problem, d is the length of the link, and i denotes the individual link. Minimizing the weight helps to minimize the fuel and power requirements for the aircraft. Another way to reduce both of those is by increasing system efficiency.

Specifically, the efficiency of the morphing substructure was investigated in this research. The efficiency was defined as a ratio of the useful work output from the system to the work put into the system. The useful work output from the system was defined as

$$W_{out} = F_{exx}X_{out} + F_{exy}Y_{out} \tag{1.4}$$

where W_{out} is the work output from the system, X_{out} is the displacement in x-direction at the vertex where F_{exx} is applied, Y_{out} is the displacement in y-direction at the vertex where F_{exy} is applied, and as before F_{exx} and F_{exy} are the external forces applied in the x- and y-directions respectively.

$$W_{in} = F_{act}\Delta l_{act} \tag{1.5}$$

Equation (1.5) shows how the work in is defined, where W_{in} is the work put into the system, F_{act} is the actuator force, Δl_{act} is the change in the actuator length. The efficiency, η, was then defined as

$$\eta = \frac{W_{out}}{W_{in}} = \frac{F_{exx}X_{out} + F_{exy}Y_{out}}{F_{act}\Delta l_{act}} \tag{1.6}$$

There are limitations on stroke length for all commercial off the shelf (COTS) actuators. The stroke length of a given actuator can limit the range of motion for any given configuration. This invites an interest in the geometric advantage (GA) for any given actuator orientation and system configuration. The GA was defined as the ratio of displacements at the vertices where the external forces are applied to the

change in actuator length

$$GA_x = \frac{X_{out}}{\Delta l_{act}}, \quad GA_y = \frac{Y_{out}}{\Delta l_{act}} \tag{1.7}$$

Finally, the actuator cannot properly actuate the system if the external forces are overpowering the force the actuator is able to produce. This leads to a definition of the blocking force, B, which is the force transferred from the externally applied forces to the actuator, which impedes the actuator performance.

$$B = \frac{F_{exx} d \sin(\theta) + F_{exy} d \cos(\theta)}{Z_1 \sin(\varphi + \theta)} \tag{1.8}$$

Equation (1.8) shows that the blocking force is dependent only on the external forces and the geometry of the problem. Unlike the efficiency, the flexibility of the system does not influence the blocking force. Here φ is the angle between the actuator and the x-axis.

1.2.3 Optimization Problem. The previously defined metrics can be used to evaluate the quality of a design. Appropriately maximizing or minimizing those metrics defines the optimization problem. The objective function is going to be a weighted sum of several objectives. The goal is going to be to minimize the weight, maximize the efficiency, and maximize the geometric advantage (GA). A scalar objective function can only be stated to be maximized or minimized (typically minimized); therefore to combine them into one function, it was necessary to have negative weighting factors, r, for both efficiency and GA,

$$\min_{w,z_1,p} \left(r_1 W_{struct} - r_2 \eta - r_3 GA_x - r_3 GA_y\right) \tag{1.9}$$

where η has to be define for multiple configuration optimization as

$$\eta = \sum_{g=1}^{N_g} c_g \eta_g \tag{1.10}$$

Here N_g is the number of configurations being considered, c_g is the weighting factor for configuration efficiency, and η_g is the efficiency of each individual configuration. Also seen in Eqn. (1.9) are the design variables. The first set of design variables, which influences both the weight and efficiency was w, the width of the individual links. The second set of design variables was z_1, which is a length that describes the actuator orientation. This single length variable was used to describe the actuator orientation because the actuator length was set to a prescribed constant length, and therefore the other mounting location, z_2, can be determined using the law of cosines. The third set of design variables, p, was used to determine which cells have active actuators and were used only in multiple-cell optimizations. This power factor, p, was a variable ranging from 0 to 1 which was cubed and multiplied the actuator force to mimic an on or off condition for each of the actuators. The constraints for the optimization problem are stated mathematically as

$$\begin{aligned} & F_{act} \geq B \\ & \sigma_i < \sigma_{\max} \\ & 0 \leq p \leq 1 \\ & \sum_{j=1}^{N_{cells}} p_j \leq N_{act} \\ & 0.1 \cdot d \leq Z_1 < Z_3 \\ & w_i \geq w_{\min} \end{aligned} \tag{1.11}$$

The first constraint is that the actuator force be at least as large as the blocking force so that the system is able to correctly actuate. The second constraint is that the individual link stresses, σ_i, be less than the maximum allowable stress of the material used, $\sigma_{\max}$. The third constraint is a side constraint defining the range of allowable values for the power factor design variables. The fourth constraint ensures that the number of active actuators is less than or equal to the number of actuators allowed in the system design, N_{act}. To do this, the power factors, p, are summed over the number of cells, N_{cells}. The fifth constraint ensures the feasibility of actuator orientation. It

is a side constraint on the actuator orientation design variable, so that an infeasible design cannot be used. The sixth constraint is a side constraint on the link widths, stating that they cannot be less than some prescribed minimum gauge length, $w_{\min}$.

This optimization was then done over each of the five different morphing configurations and several loading conditions. Just like the design of modern aircraft, optimizing the distributed actuation system of the substructure for just one configuration and loading condition means that the other configurations are going to suffer. Until adaptive actuation systems are developed, this will always be the case. Optimizing over the full range of configurations and loading conditions that aircraft will operate under will give the best possible overall solution, mitigating, as much as possible, the losses due to actuation distribution efficiency.

1.3 Overview

Determining the optimal distribution and orientation of the actuation system can be broken down into two main parts. There is the optimization routine itself and there is the objective function evaluation routine. The optimization routine is a sequential quadratic programming(SQP) technique written in `Matlab`® . The objective function evaluation is a finite element analysis (FEA) problem, as displacements are needed to calculate the objective function. The skin is a nonlinear elastic skin and the deformations involved can be large enough that the actuator force does need to move with the structure. Therefore, this is a nonlinear FEA problem, having both geometric and material nonlinearities. The nonlinear nature of the problem lends itself to be done using MSC NASTRAN™ nonlinear solution. A `Matlab`® script was written to call MSC NASTRAN™ to conduct the FEA and use the results to calculate the objective and constraints. The optimization could not be done in NASTRAN™ alone as it is unable to handle nonlinear analysis in the optimization solution sequence.

Both the optimization routine and the finite element model (FEM) needed to be validated. Experiments were used to do the validation. A single-cell experiment was designed, built, and run. This experiment was used to validate the FEA results. In

the experiment a single design variable, actuator orientation, was incrementally varied and measurements were taken and used to calculate the efficiency at each incremental actuator orientation. The results were used to verify that the SQP optimization routine was finding the same optimal orientation of the actuator.

In addition to the single-cell experiment, a three-cell experiment was designed as well. The three-cell experiment was designed to be a scaled portion of the N-MAS aircraft. Finite element models for the N-MAS aircraft were provided by NextGen for use in the scaling process. Rigorous care was taken in scaling the three-cell experiment so that it would closely relate to the actual aircraft being studied. The scaling was completed by doing an optimization using linear analysis within MSC NASTRAN™. The input files for the optimization itself were created using a combination of `Matlab`® and FEMAP, for pre and post-processing. The result was a smaller scaled portion of the N-MAS substructure, that had a similar in-plane flexibility distribution, which could be used in a three-cell experiment.

1.4 Implications

Reducing the aircraft weight and improving the efficiency of the morphing substructure will obviously increase the overall efficiency of the aircraft and eventually contribute to making morphing aircraft at the full-scale a feasible concept. The mechanization required to make the wings change shape take up much of the interior space of the wing. This interior volume is used for fuel storage on a typical aircraft. This loss of space, together with the added weight of the additional substructure, make fuel consumption and efficiency absolutely critical. Furthermore, the morphing technology is being looked at for unmanned aerial vehicles (UAV), which are not limited in mission duration by a human in the cockpit, but rather by energy requirements. Developing a more efficient morphing substructure will make application at a larger scale more feasible, and in the end provide longer mission durations. During a recent AIAA Structures, Structural Dynamics, and Materials conference president of NextGen Aeronautics, Dr. Jayanth Kudva, gave a keynote presentation on the N-

MAS aircraft, in which he identified "the optimization of distributed actuation as an area of research *critical to the success of morphing technology.*" This research contributes an understanding and quantification of the impact distributed actuation systems have on adaptive structures in general. It is one of the areas necessary for successful morphing aircraft, but other areas, such as flexible skins, also need to be researched thoroughly as well.

II. Literature Review

It was previously suggested that the morphing concept dates back to the Wright brothers and their Wright Flyer, but morphing has been around a lot longer than that. Morphing already exists in nature. For instance, chameleons can change color to blend in with their environment, or puffer fish, as seen in Fig. 2.1, are able to dramatically increase their size to scare away predators.

The interest in this research is with morphing aircraft though, and that also is currently being done. Modern aircraft use flaps, leading edge slats and flaps, and even a retractable landing gear to change the shape of the aircraft in a way that will be beneficial to the aerodynamic characteristics [8]. Researchers are more interested in large shape changes like the puffer fish and, as the current paint scheme of many fighter aircraft was inspired by fish (dark on top and light on bottom), researchers are again looking to nature for inspiration on morphing wings. As seen in Fig. 2.2, bald eagles are able to accomplish several of the goals of morphing wings. They are able to achieve both large in-plane deformations, as well as airfoil shape changes, such as camber.

To get to the point where such large deformations were possible for aircraft, many incremental steps were made first. This chapter highlights some of those important developments that laid the foundation for this research.

2.1 Adaptive Structures in Space

One of the early drives to develop an adaptive structure was for use in space. Most often large space structures, such as antennas are designed using truss structures. These structures require a high degree of precision, and in the mid to late 80s, research were looking to adaptive structures to help provide that much needed precision. There were two primary ways that adaptive structures were thought to provide added precision. The first way was through precise displacement output control of particular points. Since these structures were so large, actuators were not able to be effectively used in the traditional sense. So researchers [3, 4] looked at leveraging

(a) (b)

Figure 2.1: (a) Spiny puffer fish before morphing. (b) Spiny puffer fish after morphing to scare away predators [27].

Figure 2.2: A bald eagle is able to achieve large shape changes for different portions of the flight envelope [7].

the relatively small displacements of traditional actuators through the use of adaptive structures. The second and more predominant use of adaptive structures in space was to create a prestress. The inherent slack in the joints of the space structures added an unacceptable margin of error. Correctly placed actuators in these adaptive structures put a prestress on the joints, and therefore removed any joint looseness that would degrade the accuracy of the structure.

Once adaptive structures began being used to control precision displacement and prestressing to remove joint looseness, it wasn't too long before optimizing where to put the actuators was examined [4]. Actuator placement sought to maximize the precision, while also minimizing required input energy. For cases of prestressing, the goal was to minimize the necessary stroke length needed to keep each member of the truss in either compression or tension.

2.2 Adaptive Structures in Aircraft

After the space community showed some success with adaptive structures, the aircraft community quickly followed. Programs like the mission adaptive wing (MAW) and the active flexible wing (AFW) sought to employ these new concepts. The MAW used leading and trailing edge control surfaces to change the camber of the wing. This wing utilized flexible skins to eliminate the discontinuities between the main, stationary portion of the wing and the control surfaces. The aerodynamic advantages of this design were seen during the flight tests of the F-111 that was modified with MAW. The problem was that the mechanical actuation system it took to make the MAW work added a significant increase in aircraft weight, and therefore was not made operational [20]. The AFW utilized the control surfaces by imparting additional aerodynamic loads on a wing that was intentionally designed to be more flexible. This was done to be able to achieve a controlled aeroelastic twist. The problem with this design is that the aerodynamic performance benefits were offset by the added drag the control surfaces caused.

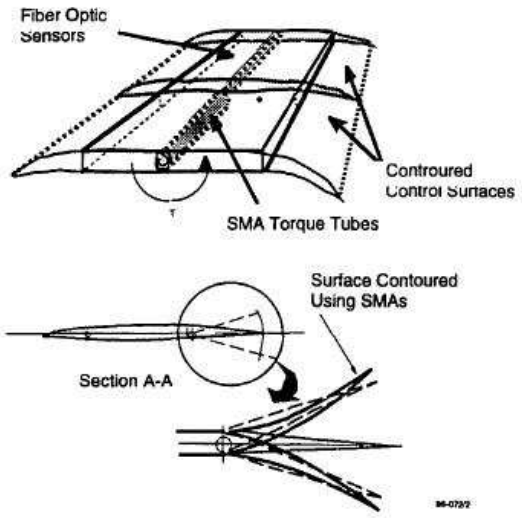

Figure 2.3: The "smart wing" uses advanced smart materials to change shape [20].

Although neither the MAW or the AFW was fielded, they laid an important foundation for future morphing wing projects. One of those projects to follow was the "smart wing" that was developed as a result of a combined Defense Advance Research Projects Agency (DARPA), Wright Lab, and NASA effort. The downfalls of earlier programs were already identified as being the weight and complexity of the actuation system, and the "smart wing" hoped to alleviate these issues by incorporating recent advances in materials, actuators, and sensors. The "smart wing" used smart materials in two different ways to achieve the intended shape changes, as seen in Fig. 2.3. First, the wing used two concentric torque tubes with imbedded shape memory alloy (SMA) to be able to twist the wing. This was able to produce 1.25 degrees of twist at the tip, which resulted in about 8% increase in roll moment during wind tunnel tests [20]. The second use of smart materials was in the control surfaces. The MAW program showed that smooth contoured control surfaces added a great benefit, so the "smart wing" tried to do this in another way. SMAs were imbedded in the top and bottom layers of the control surface composites. These SMAs were then able to apply a tensile force on either of the two surfaces, creating a hingless control surface. This hingless control surface significantly improved the pressure distribution of the wing by delaying flow

Figure 2.4: The MXF-1 can be seen here at the Camp Roberts Flight Test Range [11].

separation, which ultimately increased the overall lift. During wind tunnel tests, the hingless control surface produced 8-18% increase in roll moment [20]. This design also increases the lift reversal speed by about 20% [14]. The hingless design offers benefits beyond the enhanced aerodynamic performance. It can reduce both the radar signature and the visibility. The sharp edges and flat vertical surfaces reflect both light and radar, so the absence of the traditional hinged control surfaces reduces is highly desirable for stealth [14]. Although the "smart wing" was fairly successful during wind tunnel testing, it still was not very feasible when scaled up to full aircraft size.

The "smart wing" was successful in utilizing smart materials, and this lead to more research into potential uses of these new smart materials. Shape memory polymers (SMP), dynamic modulus composites (DMC), and dynamic modulus foam (DMF) were among the various newly developed materials that were incorporated into morphing wing designs. These materials are capable of being softened, reshaped, and made rigid again over an infinite number of cycles. They can also change volume by up to 400% [22]. These materials were primarily used to make changes in the chord of an airfoil. To accommodate large in-plane shape changes in the wing, these new materials would have to also be used in the skin of the wing.

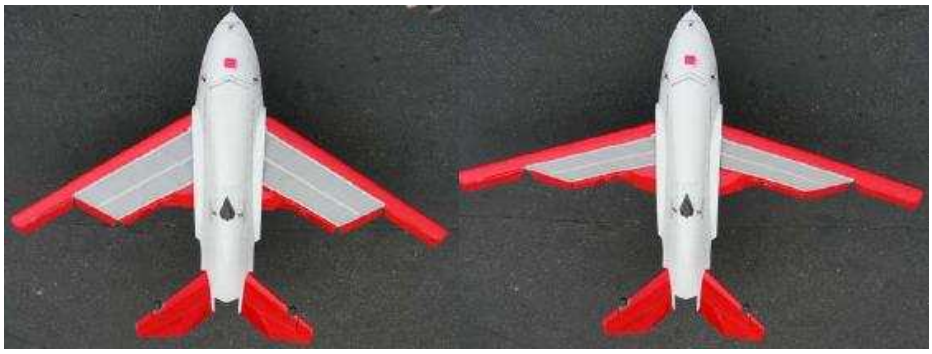

Figure 2.5: The two extreme configurations of the MXF-1 can be seen in this top view [11].

Wrapping a skin around a wing that undergoes great size changes has been one of the technological hurdles of the morphing wing design. The skin of a wing has to be able to carry significant out-of-plane aerodynamic loads. It also has to be able to keep the shape of the airfoil without any ripples, wrinkles, or excessive waviness. Furthermore, in a traditional wing the skin provides a means for shear flow which adds much needed torsional rigidity to the wing. Without this added stiffness the wing can experience much lower and more dangerous flutter speeds. NextGen Aeronautics has developed a design which overcomes the obstacles. Their proprietary flexible skin design is able to withstand over 100% in-plane strain and carry out-of-plane loads up to 400 psf [6]. This new flexible skin design is what has allowed them to design, build, and test the N-MAS model. To show actual flight performance of the morphing substructure and the new flexible skin, NextGen built a remotely piloted vehicle named Morphing Flight-vehicle Experiment (MXF-1), which can be seen in Figs. 2.4 and 2.5. The jet powered aircraft weighed 100 lbs, had a wing span of 9.3 ft, and a length of 6.8 ft. This was a single-degree-of-freedom system that was successfully able to change wing area by approximately 40%, span by 30%, and varied sweep from 15 to 35 degrees [11]. Flight tests were successful for the small-scale aircraft, but this still was not scalable to a full-size aircraft. To get a design that is feasible on the fielded level the weight and efficiency of the morphing substructure would have to be addressed. This is currently being addressed using various optimization approaches.

2.3 Optimization Efforts

Weight is always a a concern when designing an aircraft system. It needs to be minimized so that there is a lower fuel and thrust requirement. When it comes to UAVs, efficiency is also a primary concern. As the aircraft gets smaller, there is less space for energy storage. Previous research [19] has shown that these two efforts compete against each other in an adaptive structure. The effort to reduce weight cause a removal of material and that makes the structure more flexible. Increased flexibility reduces the efficiency with which the adaptive structure is able to change shape. This is because some of the energy from the actuation system goes into strain energy of the substructure. This stored energy does not get used to correctly actuate the system. When the system is made more rigid, more of that actuation energy is transferred into straining the flexible skin, allowing the substructure to change shape. Therefore, the effort to optimize both weight and efficiency is a tradeoff study and the balance of the two is left up to the decision of the designer.

Prock et al studied efficiency optimization for airfoil shape change [23]. Their goal was to find the minimum required energy input to obtain the required change in lift coefficient. This research led to the belief that new optimization techniques were needed that include multidisciplinary metrics, such as strain energy, lift, and drag.

Up until this point, aerodynamic optimization and structural optimization had been considered separately. The aerodynamics team would come up with an optimal shape for each design point in the flight envelope, and then hand those shapes off to the structures team. It was then the responsibility of the structures team to come up with an optimized structure that would occupy the given volume and be able to achieve all the necessary shapes. This was not the best approach though, because the optimal aerodynamic shapes were being achieved at the cost of high structural weight. So, research was done to combine FEA tools like ANSYS™ NASTRAN™ and ASTROS™ utilizing their internal weight optimizers with more programmable optimizers like `Matlab`® [15]. This initial research led to Maute and Reich's research

efforts to achieve multidisciplinary topology optimization of airfoil shape control [21] and Inoyama et al's in-plane shape control [17], using both finite elements software and optimization software. Although the resulting designs produced by those methods are radically different from current wing design, they do demonstrate that adaptive wing optimization does not have to be a two-step process, considering the aerodynamics and structures separately. Before both steps can be combined into one reliably, optimization methods for adaptive structures in both disciplines need to be fully developed.

Previous research [13, 19] on the optimization of distributed actuation for in-plane morphing was limited to single configuration, single loading condition, and linear analysis, with experimentation done only with a rigid test setup. A morphing wing can achieve multiple configurations and therefore needs to be optimized over all the designed configurations. Each of these different configurations correspond to different aerodynamic loads and that, along with different flight conditions, leads to many different loading conditions. The flexible skins in use, particularly in the N-MAS model, can have highly nonlinear material properties. The in-plane morphing wings can also achieve large displacements, which leads to geometric non-linearities. So, with both geometric and material nonlinearities present, it is important to include them in the FEMs used by the optimization routine. Since weight is one of the major hurdles of large deformation morphing wings, material needs to be taken out of the system and that means more flexibility. So flexible experiments to validate the optimization routine and FEM are an important step. These are the steps that this research attempts to address. Multiple configurations with multiple loading conditions for a flexible design were optimized utilizing nonlinear finite element techniques. An experiment with a flexible structure was conducted to validate the simulation.

III. Methodology

This research consisted of both analytical analysis and experimental analysis. Analytical models were first built using `Matlab`® and MSC NASTRAN™, and those models were refined to more closely match the physics of the experimental setup. The experimental data was used to validate both the finite element model and the optimization routine. After experimental validation, the analytical models were then used to obtain optimization results not easily found through experimentation.

3.1 Analytical Analysis

3.1.1 Finite Element Analysis. Accurate and fast results were dependent on accurate finite element models for input into NASTRAN™. The one-cell model was a 4-bar linkage with revolute joints that connected each of the links as seen in Fig. 3.1. The 4-bar linkage was pinned at the top vertex and the bottom vertex was only allowed to move in the y-direction. Forces were applied at the bottom and right vertices as shown in Fig. 3.1. The biggest simplification going from the wind tunnel model to the experiment and the finite element model of the experiment was modeling the skin. As seen in Fig. 3.2, the flexible skin of the N-MAS aircraft was attached in long spanwise strips. It was assumed that the flexible skin added a negligible amount of bending stiffness to the ribs and spars, so only the stiffness added to the mechanization of the substructure was modeled. The proprietary skin used for the N-MAS wing has nonlinear elastic material properties, so to correctly model the skin stiffness a nonlinear spring was made out of silicone rubber sheeting, EL 80, from Torr Technologies [1]. The nonlinear stress-strain curve for this material, seen in Fig. 3.3, was used to create a table in NASTRAN™ to capture the nonlinear material properties. All values of negative strain had zero stress. This was done so that the spring would not add any stiffness when in compression, but would add stiffness when in tension. The spring was then modeled using a CROD element with the cross-sectional area chosen to give the rod element an axial stiffness of the desired spring stiffness constant. The spring was attached between the left and right vertices,

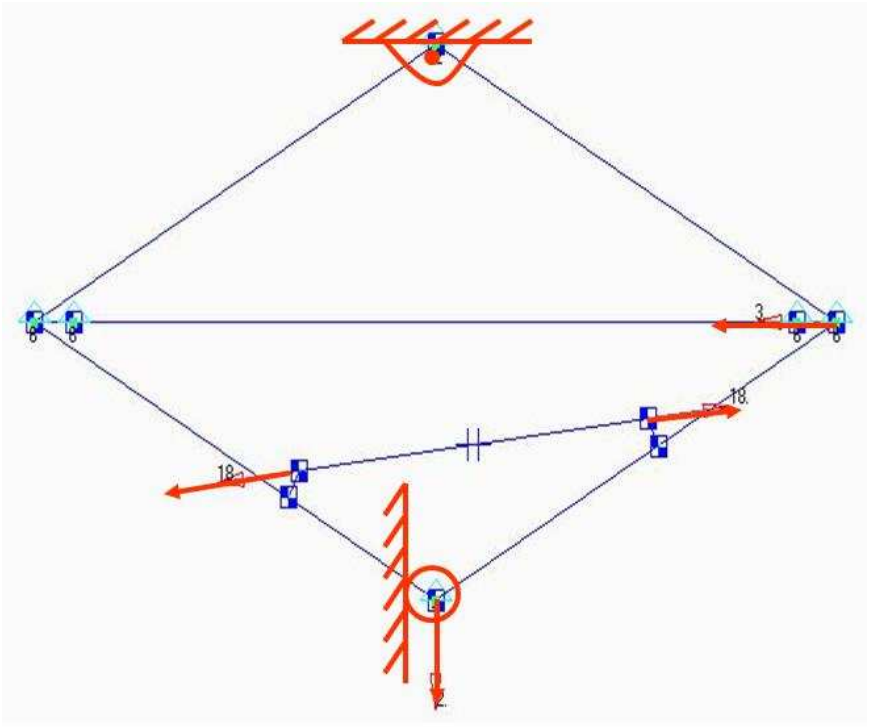

Figure 3.1: Finite element model of the single cell experiment.

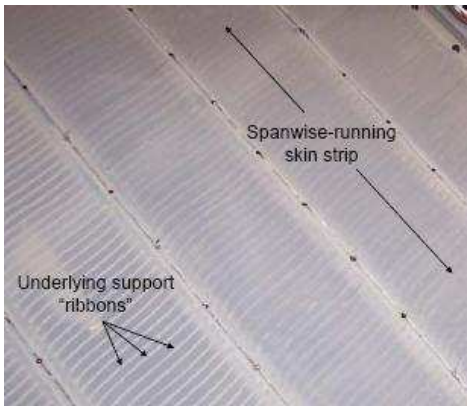

Figure 3.2: The flexible skin is attached to the N-MAS wind tunnel model in long spanwise strips [2].

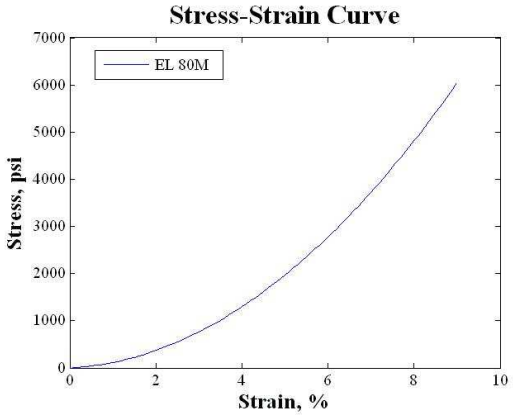

Figure 3.3: The Stress-Strain curve for EL 80M is nonlinear [1].

but the spring material could not be attached directly to the revolute joints, so it had to be offset from the joints. It was chosen to have a 1 inch offset on either side, and this offset was modeled with rigid elements in the FEM. The rigid elements connected the x and y translational degree-of-freedoms, but not the rotation about the z-axis. This caused problems for the numerical solver in NASTRAN™. The spring was essentially a string, and did not add any rotational stiffness at the node where the rigid elements attached to the spring. This caused a stiffness singularity at those nodes. Therefore, the rotational degrees-of-freedom were constrained to zero at the nodes pertaining to the spring. This was not going to affect the solution because when the spring is in tension, these degrees-of-freedom are going to be zero. Cases where the spring was not in tension, the mechanism is collapsing, and these were not of interest to this study.

All of the 4-bar linkages were modeled using CBEAM elements with a rectangular cross-section. The rotational degrees-of-freedom about the z-axis at both ends of the ribs were released so that the joints of the links could act as revolute joints. Friction in the revolute joints was not considered due to a few design implementations discussed latter, which removed enough joint slack and friction that it was considered negligible. Binding was also not considered as there were no out-of-plane loads to cause it.

An actuator was attached to two adjacent linkages, which caused the 4-bar assembly to change shape. The actuator was initially modeled as a pair of forces acting on the structure in opposite directions. This caused some problems with the numerical solver. It allowed for a mechanism in the model, because there was no stiffness added to keep the mechanism from collapsing. So, a gap element was added to represent the actuator. This gap element did not add any stiffness when the actuator forces were correctly actuating the system, but in cases where the blocking force overcame the actuator force and the system was trying to collapse, the gap element was closed and compressive axial stiffness of the actuator was taken into account. Initially the stiffness of the gap element was calculated based on the compressibility of the air in the actuator. This stiffness was too low though, and still allowed for mechanisms in the model. If the actuator is closed off to the air supply system, then this is an accurate way to model the compressibility of a pneumatic actuator, but in cases where the air delivery system is not closed off from the actuator this may not be correct. The actuator used in the experiment was not closed off from the delivery system and research has shown that if the air supply system has the same or larger volume of air than the actuator, then the actuator provides only a negligible amount of compressive stiffness [10, 26]. If hydraulic fluid were used instead of air, then this would not be the case, or likewise if a different type of actuator, such as a power screw, was used. So, to deal with the mechanism in the FEM, a sufficiently large stiffness was given to the gap element. This again did not affect the results because it was only a factor when the system was collapsing and post-collapse response was of no interest.

The boundary conditions and forces applied can be seen in Fig. 3.1, drawn in red. The top vertex is pinned, while the bottom vertex is constrained not to have any displacement in the x-direction. A force in the negative y-direction, F_y is applied at the bottom vertex and a force in the negative x-direction, F_x, is applied at the right vertex. A gravitational force is applied to the entire system so that the influence of weight could be accounted for. The gravitational acceleration was in the negative y-direction. For the gravitational forces to be correct, the masses had to be accurate.

All the hardware used to assemble the experiment was weighed and modeled as point masses. Gap element properties do not allow for any mass, so the actuator mass was modeled as two point masses, with half the mass placed at each of the mount points. The spars and ribs were modeled as constant cross-sectional rectangular elements and this did not capture the actual shape of these elements. The actual linkages had different geometries at the joints to accommodate assembly of the system and these differences were not captured in the FEM. So to adjust for this, the entire experiment was weighed and then the mass density of the aluminum material was adjusted until the FEM weight matched the measured weight.

3.1.2 Optimization Routine. The objective for the optimization was to minimize structural weight and maximize both the efficiency and the GA of the distributed actuation system, Eqn. (1.9), while satisfying the constraints in Eqn. (1.11). The optimization was done completely with `Matlab`® . The outermost loop was written by Mark Spillman and Dr. Robert Canfield and was based on Schittkowski's Sequential Quadratic Programming (SQP) method [25]. The SQP code calculates the objective function gradients and constraint gradients using an internal forward finite differencing method. This outer loop SQP program calls another `Matlab`® script that does the objective function and constraint evaluations. The script that does the evaluation has three different parts. The first part is to write out NASTRAN™ input files based on the current evaluation point. Following that the script uses those input files to run MSC NASTRAN™ nonlinear analysis. The third part of the function evaluation script is to read in the necessary output from the NASTRAN™ analysis and calculate both the objective function and the constraints based on the FEA results. These three parts were contained in a loop so that all three were done for each configuration. The FEA could be done once for all the loading conditions of one configuration, but to do the analysis on different configurations, different input files had to be created. The function evaluation would then compute the weighted sum of efficiencies and structural weight for all the load case and configuration combinations desired.

The function evaluation script had to be robust enough to handle two difficult situations. The first was if the SQP outer loop optimizer was trying to evaluate a configuration that was not geometrically feasible. If this were the case, the function evaluation script would end, and send back to the optimizer a highly undesirable result for both the objective and the constraints. The second difficult case had to do with the FEA. Because the FEA was nonlinear, there were times when the result would not converge before it ended. The function evaluation script had to be able to identify when this was the case and then, more importantly, adjust the nonlinear analysis parameters so that convergence could be achieved.

The nonlinear analysis parameters that the `Matlab`® code adjusted are those used by NASTRAN™to determine how to solve the system of nonlinear equations. This FEA contains both geometric and material nonlinearity so two important solution techniques in NASTRAN™ are important to understand. The first concept is load increment. At the outer most loop of the nonlinear solution sequence, NASTRAN™ will divide the applied loads into a number of incremental loads. These smaller incremental loads, if small enough, will result in a more linear response. The idea is to keep the strains and displacements small at each increment. This is done for both the material and geometric nonlinearity. Then within each of these load increments, the set of nonlinear equilibrium equations is solved

$$[K(u)]\{u\} = \{P(u)\} \tag{3.1}$$

where K is the stiffness matrix which is a function of the displacements, u, and P is a vector of the applied nodal loads which is also a function of the displacements. These nonlinear equilibrium equations are solved in NASTRAN™ using the Newton-Raphson method [9]. The Newton-Raphson method is and iterative solution method. So, the first step is to make the nonlinear equilibrium equations iterative,

$$\left[K(u^i)\right]\left\{u^{i+1}\right\} = \left\{P(u^i)\right\} \tag{3.2}$$

showing that the displacements being solved for in this iteration depend on the displacements resulting from the last iteration. The next step is to define a residual function to measure the accuracy of the current iteration,

$$R \equiv P - K(u)u \tag{3.3}$$

where R is the residual function after each iteration. The residual is then approximated using a Taylor Series expansion,

$$R(u^i) = R(u^{i-1}) + \left.\frac{\partial R}{\partial u}\right|_{u=u^{i-1}} \Delta u^i + ... \tag{3.4}$$

where the step size between iteration, Δu is defined as

$$\Delta u^i \equiv u^i - u^{i-1} \tag{3.5}$$

The goal of the Newton-Raphson method is to iterate until either the residual function is below a prescribed tolerance and thus providing the answer, or the step size is below a prescribed tolerance and the solution has not converged. The number of iterations allowed can be controlled by the user. The stiffness matrix as shown in Eqn. 3.1 is a function of the displacements, so it has to be updated as the displacements are updated. The number of iterations that are solved before the stiffness matrix is updated is controlled by the user as well. If the stiffness is updated every iteration then this is considered the Modified Newton-Raphson Method. The stiffness updates takes care of the material nonlinearity and is part of the solution for geometric nonlinearity. The other part to geometric nonlinearity is taken care of in the force vector, which is also a function of the displacements. After each load increment the individual element coordinate systems, known as the Lagrangian reference frame, are update to reflect the new displacements. Updating the Lagrangian reference frame calls for the stiffness matrix to be updated and the force vector being updated. This takes care of geometric nonlinearities due to follower forces and large displacements.

The parameters for nonlinear static analysis control are found on the NLPARM input card in NASTRAN™. There were five of these parameters that the function evaluation script would change as needed. The first was the number of increments, NINC, that the load was divided into. This was increased to allow convergence. The second parameter was the method by which the stiffness matrix was updated, KMETHOD. Ordinarily the method was set to AUTO, but upon detecting non-convergence, it was changed to ITER, which means that the stiffness matrix was updated after a set number iterations. That set number of iterations before the stiffness matrix was updated, KSTEP, was the third parameter, and it was decreased to better allow for convergence. The fourth parameter was the maximum number of iterations per load increment, MAXITER, the numerical solver could complete. This was increased to allow convergence. The fifth and final parameter was the maximum number of bisections, MAXBIS, allowed for each load increment, and it was increased to allow convergence. These parameters greatly influence whether or not a converged solution is achieved, as well how long it takes to converge. Therefore, the function evaluation script was written to incrementally change those above parameters as needed, but then to also set them back to the original values when possible to allow faster solutions.

3.2 Experimental Validation

3.2.1 Single-Cell Experiment.

3.2.1.1 Design. The design for the single-cell experiment was driven by time requirements and the desire for simplicity. A predetermined amount of flexibility was used in the single-cell experiment. The predetermined efficiency loss due to added flexibility was 20% of the efficiency in the rigid case. The first step was to determine the efficiency of a rigid system. The rigid system is not going to achieve 100% efficiency, even if factors such as joint stiffness were neglected, because much of the work input is going to strain energy in the nonlinear spring, and this is not

captured in the work output as defined in Eqn. (1.4). A nonlinear FEA was performed using essentially rigid ribs and spars. The interior half angle was 45 degrees and the actuator was oriented parallel with the spring and set to a length of 10 in. The actuator force was set to be 14 lbs and the external forces were 3 lbs in both the x-direction and y-direction. The efficiency was calculated to be 56.39% with only 0.38% of the total strain energy going to deforming the substructure. The experiment was then to be designed to have 80% of this efficiency for the same setup.

A simple optimization was completed to come up with a design that met this goal. Designing the the experiment did not need to be done as an optimization, but it was used as a chance to test the optimization routine, the FEM, and more importantly the interaction between the two. The objective function was to minimize the difference between the actual and desired system efficiency (45.11%, i.e., 80% of the rigid efficiency). There was only one design variable and that was the thickness of the rib that the actuator was attached to. The rest of the dimensions were set based on what was needed for proper assembly of the experiment and manufacturing costs. There were no constraints for this optimization. The optimization was a success, but it resulted in a rib thickness that was between two nominal sizes. In the interest of manufacturing costs, the intent was to design the experiment using nominal dimensions so that stock aluminum was readily available and could be used with minimal machining needed. Therefore, 0.125 in and 0.0625 in were looked at for the experiment. For each case a FEA was completed using these nominal rib thicknesses. For the case of 0.125 in, the efficiency was 53.85% (97.5% of rigid efficiency) with 15.83% of the total strain energy going to deforming the structure. In the 0.0625 in case, the efficiency was calculated to be 33.78% (40.0% of rigid efficiency) and 80.10% of the total strain energy going to deforming the structure. While running the experiment, there were three measurements that needed to be taken, X_{out}, Y_{out}, and Δl_{act}, at the location shown in Fig. 3.4. These displacements were examined for each of the FEAs done on the proposed experimental design to ensure that they were on a magnitude that was measurable by the intended methods. They were

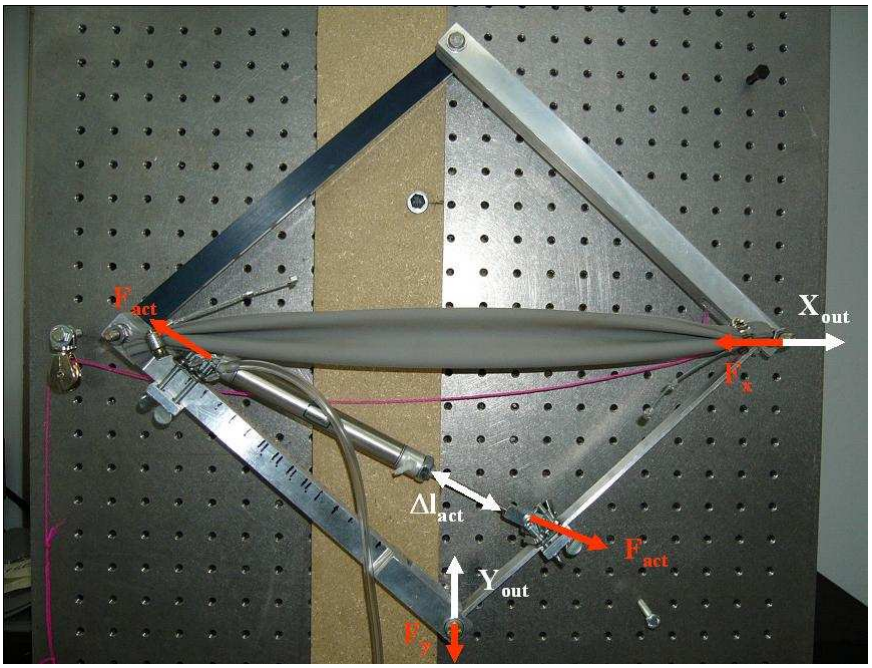

Figure 3.4: Closeup of the single-cell experiment.

determined to be on the order of 2 in, which was well within the measurable limits. The final dimensions of the experiment, seen in Fig. 3.4 can be found in Table 3.1. The dimensions reported for the links are the measurements at the center of the link. As seen in Figs. 3.4 and 3.5, there are different dimensions at the joints. This was done for assembly purposes, but the dimensions reported in Tbl. 3.1 were used for the FEM.

Previous research where similar experimentation was done [13] did not achieve results that matched predicted values as well as hoped. This was in part due to joint stiffness not captured in the mathematics of the analysis. To mitigate the influence of the joint stiffness, special care was taken in designing the joints and the experiment assembly. The joint was designed so that the flexible rib would be assembled such that it was sandwiched between two parts of the spar. This can be seen in Fig. 3.5. Boca bearings, part number FR188-ZZ, were also used to lower the stiffness of the joint. Two bearings were used in each joint, which were press fit into the outside of each side of the spar.

Table 3.1: These are the design specifications of the single-cell experiment.

Variable	Value
Material of links	7075 aluminum
Material of spring	EL80M
d	11.5 in
Spar without actuator attached	1.0 in x 0.75 in
Spar with actuator	0.6875 in x 0.75 in
Rib without actuator attached	0.375 in x 0.75 in
Rib1 with actuator attached	0.6875 in x 0.125 in
Rib2 with actuator attached	0.6875 in x 0.0625 in
Actuator offset distance	0.5805 in
Spring offset distance	1.0 in
Starting actuator length	8.875 in
Spring stiffness	2.5 lb/in
Actuator part number	UDR-10-4
Bearing part number	FR188-ZZ

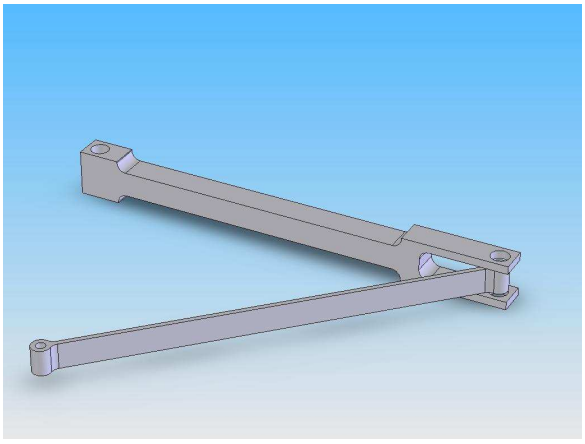

Figure 3.5: This was the joint design for the single-cell experiment. It was used in order to reduce binding friction to a negligible amount.

Figure 3.6: Single-cell experiment setup.

The links were all machined out of 7075 aluminum to keep the experiment lightweight, and the material properties are readily available. As mentioned earlier, the spring was made with silicone rubber sheeting, EL 80M, chosen for its nonlinear material properties. The thickness chosen was 0.030 in, as it was the least expensive. The sheeting was cut to length and then rolled up so that the cross-sectional area would result in the desired spring stiffness. The rolled up material was then clamped at the ends to a cable with metal stops on it to keep the spring from sliding. The cable was intentionally cut long with additional metal stops added, as seen in Fig. 3.4. This was done so that the clamped location of the spring could easily be changed, changing the length of the spring, essentially changing the stiffness of the spring. Future work could then investigate the affects of varying the skin stiffness.

3.2.1.2 Running Experiment. The experimental setup can be seen in Fig. 3.6. The mechanism was mounted vertically to a screw board at the top vertex. This joint was allowed to pivot because of the bearings in the joint. The bottom vertex was constrained in the x-direction by a piece of wood mounted vertically, and

a bearing on the screw shaft that rested against the wood. The force applied at the right vertex in the $-x$-direction kept the bottom vertex against the vertically mounted piece of wood (white piece of wood in the figure). Before the system was turned on, the bottom vertex rested on a stop (brown piece of wood next to white piece of wood), which set the initial configuration. In this position the spring had zero strain. In this resting initial configuration the length of exposed actuator shaft was measured and recorded and the distance between the right vertex and the far mounted vertical piece of wood was similarly measured and recorded. These measurements were used as the starting position of the system at rest. The left side of the actuator was mounted to the appropriate location along the left spar and accordingly the right side was mounted to the the location that kept the initial starting length of the actuator the prescribed constant starting length. The air supply was then turned on with the inline shutoff valve, and the actuator allowed to apply a force. Three measurements were then taken and recorded, if the bottom vertex rose off of the wooden stop. The new length of actuator shaft was measured. The distance off the vertical stop that the bottom vertex rose was measured. The distance between the right vertex and far right vertical piece of wood was recorded. All the values were input into a `Matlab`® script which compared the starting values and new values to calculate the displacements resulting from the actuator force. If the bottom vertex did not leave the vertical stop, then either the system was exactly in equilibrium at that point, or the externally applied forces were overcoming the actuator force and the system was trying to collapse. Either way, these cases were not of interest and the change in displacements were recorded as zero. All displacement measurements were taken with digital calipers to a precision of five significant digits.

The incoming air supply was 100 psi, and it was regulated down to the appropriate pressure using a McMaster Carr® air pressure regulator, part number 4246K61. The air was then delivered to an inline Honeywell Sensotec model Z pressure transducer. The pressure transducer was run off of a Vishay Measurements Group power supply and strain gauge conditioner, models 2110A and 2120A respectively. The out-

put from the strain gauge conditioner was read using a Fluke model 45 multi-meter, which directly read the pressure.

The actuator used was a Clippard Minimatic® actuator, part number UDR-10-4. It was chosen primarily for its size and weight. The force produced by this actuator was measured to check that the published power factor of 0.31 was accurate. The actuator force was calibrated using a Transducer Techniques® load cell, model number THB-500-R. Figure 3.7(a) shows the setup for calibrating the actuator. The actuator was placed between the table top and a wood stop, with the load cell inline. The load cell was connected to a National Instruments signal conditioning block, model SC-2345, which was in turn connected to a National instruments PX1-1042 computer. LabVIEW software was then used to convert the load cell voltage into an actual force. This setup was calibrated using know weights.

The nonlinear spring stiffness was measured by using the same load cell. As seen in Fig. 3.7(b) the spring was connected to the load cell which rested against a rigid mount. The spring was then pulled a measured displacement and the resulting force was recorded.

3.2.2 Three-cell Experiment. More time was taken with the design of the three-cell experiment, to better correlate to the actual aircraft. Much of the model was designed similarly to the single-cell, such as the actuation, mechanization, and joints, but the difference came in how the cross-sectional dimensions were chosen. Once again, the height was held to a fixed 0.6875 inches to make actuator attachment and manufacturability better. The width for each member was decided based on aeroelastic scaling methods.

The design of the three-cell experiment was done by scaling part of the wing substructure from a finite element model of the actual aircraft. The overall scaling process started with developing the necessary non-dimensional parameters to match between the two models. The next step was to apply a distributed load and boundary conditions to the full-size model and determine the response. The response was

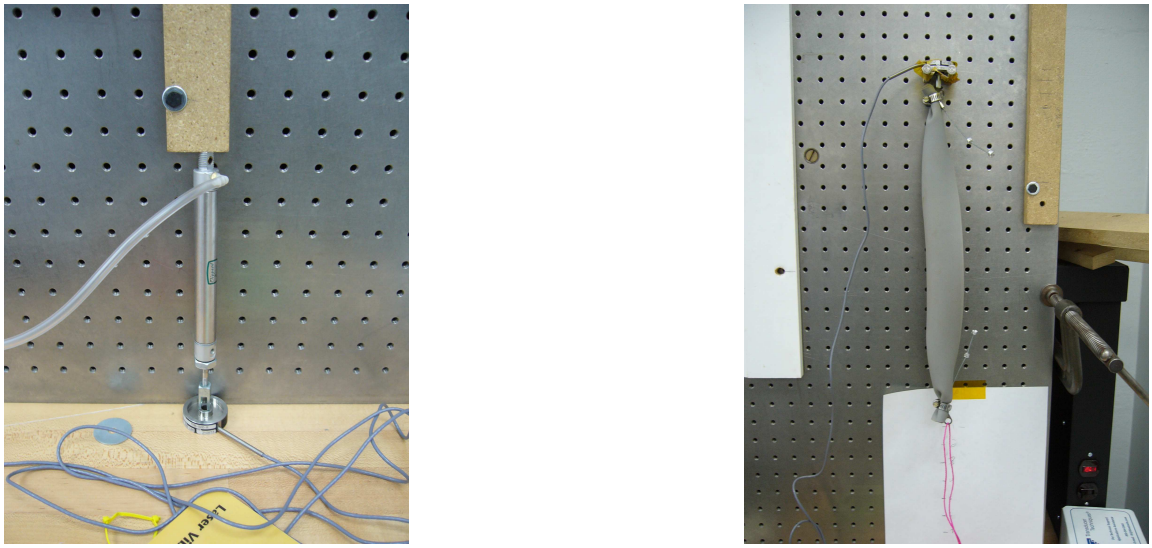

(a) (b)

Figure 3.7: (a) Actuator force was calibrated using a load cell. (b) Spring stiffness was calibrated using load cell and pre-measured distances.

then non-dimensionalized and used to match the scaled model's response. The same boundary conditions were then applied to the scaled model and the same distribution of load from the full-size model was applied to the scaled model, but scaled according to the non-dimensional scaling parameters previously determined. The distributed stiffness of the scaled model was then changed until the non-dimensional response matched that of the full-size model. The means by which the stiffness distribution of the scaled model was changed was an optimization problem following a similar method as French and Eastep [12].

The non-dimensional parameters that needed to be matched between the full-size model and the scaled model were derived from the basic finite element equation,

$$[K]\{u\} = \{P\} \tag{3.6}$$

where K is the stiffness matrix, u is the vector of displacements, P is the vector of applied modal forces.The only two elements that need to be considered were beam

elements and rod elements, as these were the only elements contained in the part of the substructure of interest to the experiment. First, consider the beam element equilibrium equation,

$$\frac{\mathrm{EI_z}}{\mathrm{L_e}^3}\begin{bmatrix} 12 & 6L_e & -12 & 6L_e \\ & 4L_e^2 & -6L_e & 2L_e^2 \\ & & 12 & -6L_e \\ & & & 4L_e^2 \end{bmatrix}\begin{Bmatrix} V_1 \\ \theta_{z1} \\ V_2 \\ \theta_{z2} \end{Bmatrix} = \begin{Bmatrix} F_{v1} \\ M_1 \\ F_{v2} \\ M_2 \end{Bmatrix} \tag{3.7}$$

where E is the material modulus of elasticity, I_z is the area moment of inertia about the z-axis, L_e is the length of the element, V is the vertical displacement at each node, θ_{z1} is the rotation about z-axis at each node, F_v is the vertical force at each node, and M is the moment at each node. Equation (3.7) was non-dimensionalized through a few steps. First, the displacements were non-dimensionalized by dividing all translation degrees of freedom by a characteristic length, L_o, and then multiplying the corresponding columns of the stiffness matrix by the same term. Next, the rows dealing with rotations were divide by the characteristic length on both sides of the equation. The force vector was non-dimensionalized by dividing the entire vector by a characteristic force, F_0, and putting the same term in front of the vector, yielding

$$\frac{\mathrm{EI_z}}{\mathrm{L_e}^3}\begin{bmatrix} 12L_0 & 6L_e & -12L_0 & 6L_e \\ & 4L_e^2/L_0 & -6L_e & 2L_e^2/L_0 \\ & & 12L_0 & -6L_e \\ & & & 4L_e^2/L_0 \end{bmatrix}\begin{Bmatrix} V_1/L_0 \\ \theta_{z1} \\ V_2/L_0 \\ \theta_{z2} \end{Bmatrix} = F_0\begin{Bmatrix} F_{v1}/F_0 \\ M_1/L_0F_0 \\ F_{v2}/F_0 \\ M_2/L_0F_0 \end{Bmatrix} \tag{3.8}$$

The non-dimensional stiffness matrix, displacements and forces were then defined as

$$\left[\overline{K_b}\right] = \frac{\mathrm{EI_z}L_0^2}{\mathrm{E_0I_{z0}L_e}^2}\begin{bmatrix} 12L_0/L_e & 6 & -12L_0/L_e & 6 \\ & 4L_e/L_0 & -6 & 2L_e/L_0 \\ & & 12L_0/L_e & -6 \\ & & & 4L_e/L_0 \end{bmatrix} \tag{3.9}$$

$$\{\overline{u}\} = \begin{Bmatrix} V_1/L_0 \\ \theta_{z1} \\ V_2/L_0 \\ \theta_{z2} \end{Bmatrix} \tag{3.10}$$

$$\{\overline{P}\} = \begin{Bmatrix} F_{v1}/F_0 \\ M_1/L_0F_0 \\ F_{v2}/F_0 \\ M_2/L_0F_0 \end{Bmatrix} \tag{3.11}$$

where the bar signifies that the term is non-dimensionalized, and the subscript b denotes it is the beam element stiffness matrix. Substituting Eqns. (3.9) thru (3.11) into Eqn. (3.8) yields the non-dimensional element equilibrium equation

$$\frac{\mathrm{E_0I_{z0}}}{\mathrm{F_0L_0^2}} \left[\overline{K_b}\right] \{\overline{u}\} = \{\overline{P}\} \tag{3.12}$$

The same type of non-dimensionalization was done for a rod element, yielding Eqn. (3.13), in which the r subscript denotes it is the rod element stiffness matrix, and A_0 is the characteristic cross-sectional area of the element.

$$\frac{\mathrm{A_0}E_0}{F_0} \left[\overline{K}_r\right] \{\overline{u}\} = \{\overline{P}\} \tag{3.13}$$

The non-dimensional terms in front of Eqs. (3.12) and (3.13) were the scaling parameters that had to be matched for the full-size and scaled models. These quantities were set for the full-size model and were decided by the designer for the scaled model. Once these terms were decided upon, the scaling could then be started by matching the barred quantities for the scaled model in Eqs. (3.12) and (3.13) to the full-scale model's values.

The scaling started with five finite element and panel flutter models provided by NextGen Aeronautics, as seen in Fig. 3.8. For a complex wing, such as the N-MAS, previous research has shown that a simple beam or single plate structural repre-

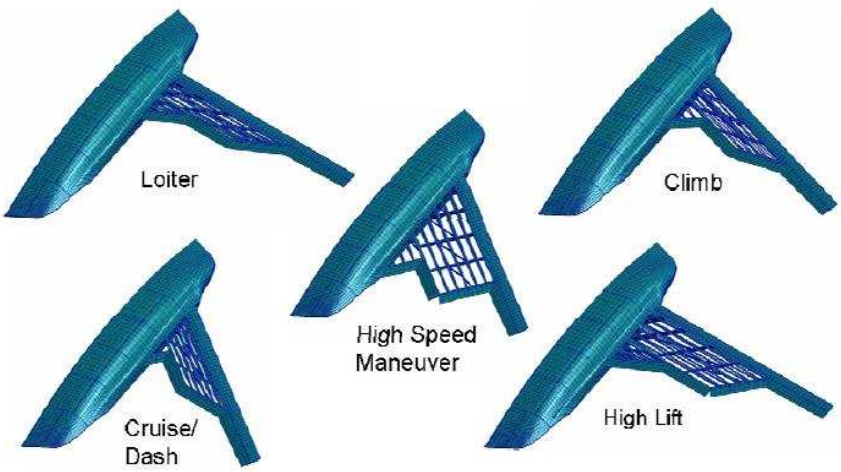

Figure 3.8: Finite element models for the five different configurations of the N-MAS [2].

sentation of the wing will not give sufficient results [14]. Therefore it was deemed necessary to use the both the structural and aerodynamic models already developed by NextGen. The aerodynamic panels for each configuration can be seen in Fig. 3.9. A static aeroelastic analysis was completed on each model using the Doublet-Lattice subsonic lifting surface method in NASTRAN™. The static aerodynamic lift loads determined by the analysis were output using the NASTRAN™ OLOADS request. OLOADS is an output request that reports all the loads applied to the model. However, these applied loads were only the out-of-plane lifting loads. The Doublet-Lattice subsonic lifting surface theory does not provide any means to apply in-plane parasite drag forces, and these are the primary forces influencing the optimal location and orientation of the distributed actuation system. Therefore, some approximations for the total drag forces were necessary. A `Matlab`® script was written to calculate the wetted aspect ratio for each of the configurations. That script used approximations for the body wetted surface area, based on the finite element model, and approximations for the wing wetted surface area using [24],

$$S_{\text{wet}} = S_{\text{exposed}}[1.977 + 0.52(t/c)] \tag{3.14}$$

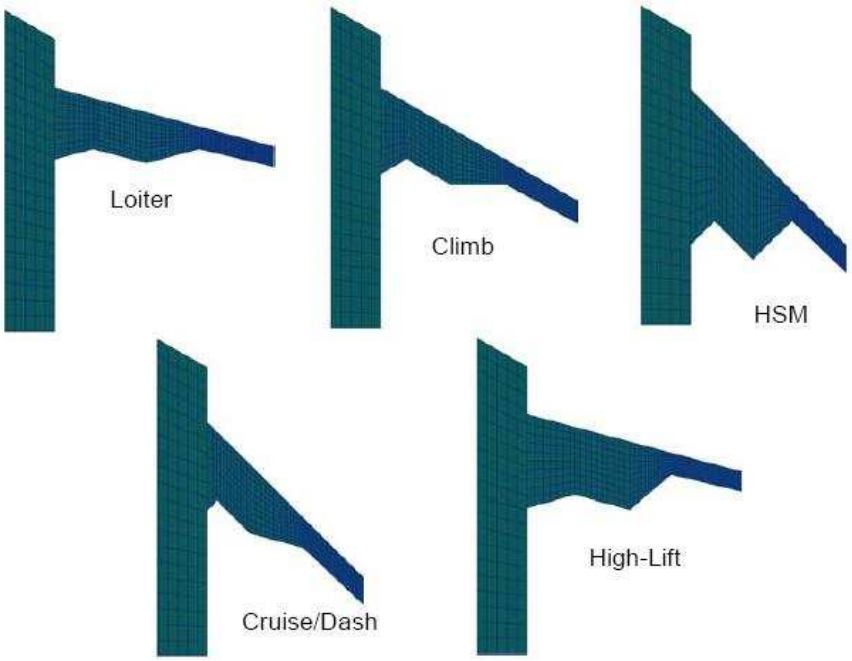

Figure 3.9: Aerodynamic models for each of the configurations of the N-MAS aircraft [2].

where S_{wet} is the aircraft wetted surface area, S_{exposed} is the wing exposed planform area, and (t/c) is the ratio of wing thickness to chord. That approximated wetted aspect ratio was then used to look up lift-to-drag ratios for each of the aircraft configurations, based on typical values for military aircraft with similar wetted aspect ratios [24]. Once the lift-to-drag ratios were approximated, they were then used along with the applied lift loads from the static aeroelastic finite element analysis to determine approximate drag loads

$$D = \frac{L}{L/D} \tag{3.15}$$

Each individual out-of-plane lift load was used in Eqn. 3.15 to determine the drag loads to be applied at the same nodes. Next, a static finite element analysis, again using MSC NASTRAN™, was done with just the in-plane loads applied to the wing. The GPLOADS output was used in NASTRAN™ so that the force balance at each of the nodes could be read. GPLOADS is an output request that prints out a grid point force balance at each of the nodes in the model.

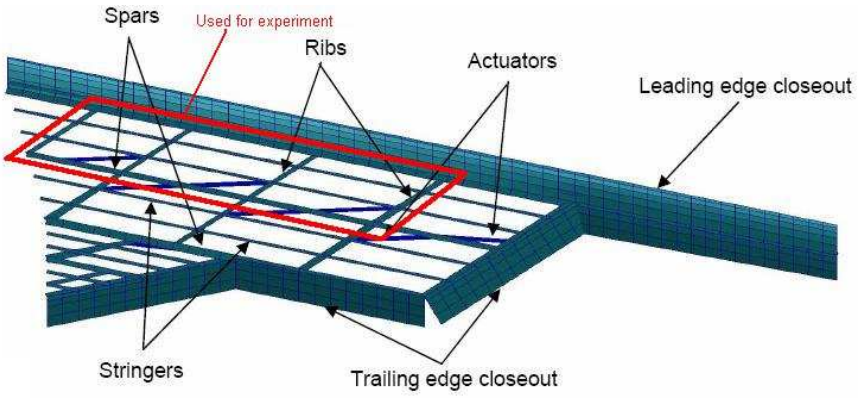

Figure 3.10: Closeup of the finite element model of the N-MAS substructure [2].

Next, any part of the finite element model that was not of concern was removed. The portion that was used to design the experiment, not including the stringers, can be seen outlined in red in Fig. 3.10. This left, as a reduced model, only the three interior cells of interest for the experiment. Then, a `Matlab`® script was used to read in all the grid point force balance loads from the complete model and any element internal load that was not in the new reduced model, but was attached to the reduced substructure, was consequently applied as an external load to the reduced model. This resulted in a reduced three-cell model that had all the loads applied to it as if were still part of the entire wing model. Figure 3.11 shows the applied loads equivalent to the full model being present. Note, that there are multiple loads at any given node, and it is not a resultant load distribution, rather each removed element contributes an applied drag force as a separate applied load. The response to that static in-plane loading was then used as the basis for the scaling. It should be noted that this complex load distribution did not need to be used for scaling purposes, nor did the approximate in-plane drag forces need to be determined for scaling. A number of nodal unit forces could have been used instead [2,5,16]. The reason for going through the trouble of determining the complex force distribution is so that actuator forces and applied external forces for the experiment can be determined such that they too relate back to the wind tunnel model.

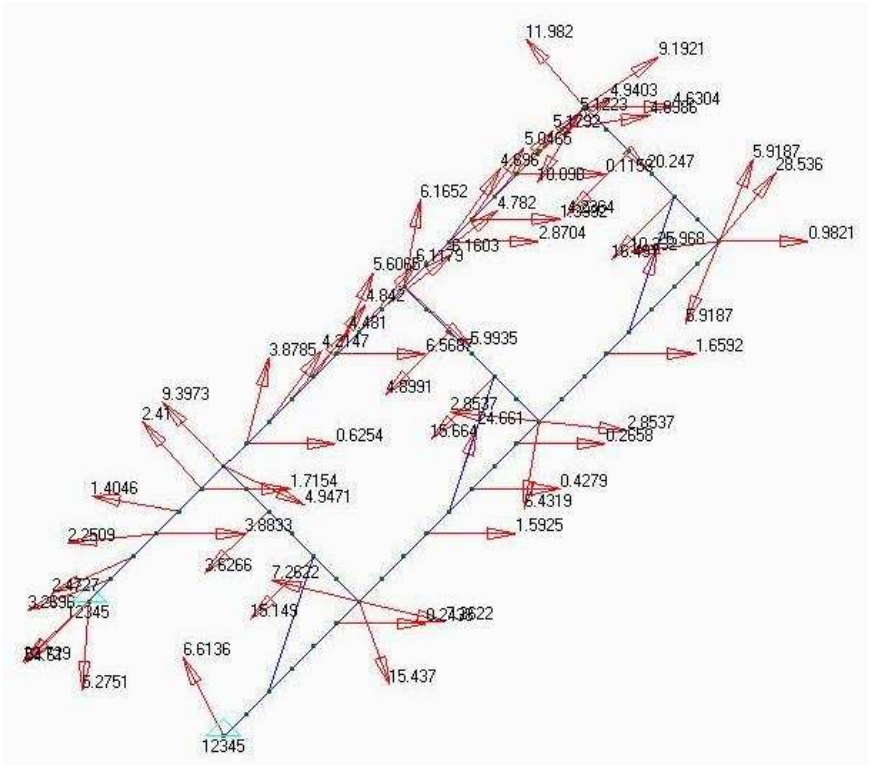

Figure 3.11: Distributed load used to scale the three-cell experiment from the N-MAS wind tunnel model.

A smaller three-cell model with the same node and element numbering was then created and the same distribution of forces was applied to it. The same node and element numbering allowed for the same nodal forces from the full-size model to be applied to the smaller model, but scaled down at a ratio that made the non-dimensional parameters in Eqs. (3.12) and (3.13) match. The smaller, reduced model was also built with simple rectangular constant cross-section members to make fabrication inexpensive and easy, whereas the full-size model had tapered I-beams and C-channels for its members.

NASTRAN™'s optimization solution was then used to complete the scaling process. A `Matlab`® script was written to take all the nodal displacements and elemental strain energies from the full-size model and write the necessary optimization input deck for NASTRAN™. The design variables were the cross-sectional widths of each member in the three-cell model, leaving the height of each fixed. The objective function was to minimize the sum of the squares of the difference between the non-dimensional displacements and strain energies of the two models,

$$\min_{w_i} \left(\sum_{n=1}^{N_n} \left(\overline{D}_{L_n} - \overline{D}_{S_n} \right)^2 + \sum_{e=1}^{N_e} \left(\overline{U}_{L_e} - \overline{U}_{S_e} \right)^2 \right) \tag{3.16}$$

where $\overline{D}_L$ are the nondimensional displacements of the large-scale model, $\overline{D}_S$ are the nondimensional displacements of the small-scale model, $\overline{U}_L$ are the nondimensional strain energies of the large-scale model, $\overline{U}_S$ are the nondimensional strain energies of the small-scale model, N_e is the number of elements, N_n is the number of nodes, e denotes the individual element number, and n denotes the individual node number.

This optimization found the closest distribution of flexibility so that the scaled displacements and strain energies matched between the two models. The flexibility distribution could not match exactly, because the full-size model had tapered members and the small-scale model had constant cross-section members. The displacements alone could not be used, because there were many different flexibility distributions that could allow the displacements to match. The influence of the stiffness matrix

was captured by forcing the strain energies to match, as well, and thereby providing a unique solution and better match of the flexibility distribution. The optimization thereby indirectly found the closest possible match of the non-dimensional stiffness matrix. This was more convenient than the alternative of minimizing the difference between the model and full-scale stiffness matrices,

$$\min \left\| \overline{K_{\text{model}}} - \overline{K_{\text{full-scale}}} \right\| \tag{3.17}$$

because the displacements and strain energies are outputs readily available in NASTRAN™ for use as responses in the optimization module. The alternative method could be used if a `Matlab`® script were written to do the optimization. NASTRAN™ provides the ability to use a high-level programming language called Direct Matrix Abstraction Program DMAP. The DMAP alteration code in Appendix A can be used in the input file for NASTRAN™ so that one of the output files will be the globally assembled stiffness matrix. This output file could then be used by the `Matlab`® script to calculate the difference in stiffness matrices. This method was not used as it would have taken more time to program the needed `Matlab`® code. The scaling optimization that was used produced cross-sectional dimensions for each of the members in the experiment.

IV. Results

Results were obtained for the single-cell experiment and shown to be very repeatable. Some of those results were used to update the FEM representing the single-cell experiment. The FEM was analyzed using non-linear static solution methods described earlier, and those results were compared to the remaining results from the single-cell experiment to show confidence in the accuracy of the FEM. Optimizations were then performed to determine what the optimal actuator orientations are for individual configurations and over multiple configurations. Finally a three-cell experiment was successfully designed by scaling part of the N-MAS wind tunnel flutter FEM.

4.1 Single-cell Experiment

There are three important measured displacements throughout the results. Those measured displacements were taken from the locations in Fig 4.1. The first step in the single-cell experiment was to repeat the experiment several times show that the data was consistent between each run. The experiment was run seven times with any where from three to nine loading conditions in each run It wasn't until the last three runs that the process was improved enough that the results were repeatable to within desired limits. The last three runs were consistent and therefore used for analysis. The results presented here are compiled from the data of those last three runs of the experiment, but the full set of data can be seen in Appendix B . Figures 4.2, 4.3, 4.4, and 4.5 are shown for the case where $\theta = 45°$, $F_{act} = 13.625$lbs, $F_x = 3$lbs, and $F_y = 1$lb. There was a maximum variation for the X-displacement measurement of 4.72%. All four figures have the actuator orientation on the x-axis. The actuator orientation can be described by one length which is the Z_1 variable described earlier. The respective measured quantity is on the y-axis. The maximum variation in Y-displacement was 5.09%. The maximum variation in actuator displacement, Δl_{act}, through these three runs was 3.02%. While the maximum variation in the three measurements taken was only 5.09%, these led to a maximum variation of 13.00% in the

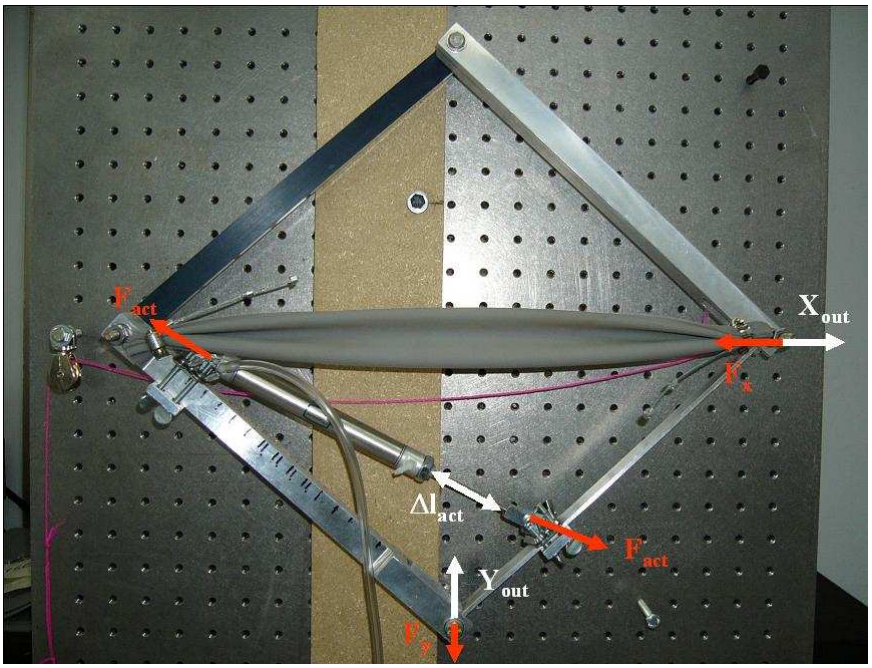

Figure 4.1: The displacements for the single-cell were taken at the locations shown here.

calculated efficiency of the system, Eqn. (1.6). The efficiency plotted in Fig. 4.5, is the average efficiency and the error bars are based on the highest and lowest calculated efficiencies over the three runs.

Before these experimental results can be compared to the FEA results, the FEM needed to be updated to be as accurate a representation of the actual experiment as possible. Two things were done to increase the accuracy of the FEM. The actuator force was measured and updated in the FEM to reflect the results, and the spring stiffness and material modulus of elasticity was done likewise. The actuator was measured with a supplied air pressure of 45.16 psi. With a power factor of 0.31 this should produce a actuator force of 14.0 lbs. The actuator force was measure three times at 1000 hz sampling rate. The results can be seen in Fig. 4.6. Using this data, a mean actuator force for each run and the corresponding standard deviation was computed, Table 4.1. The last line of the table shows the results for all the data from each of the runs combined. The small and constant variations are due to the data collection system, such as supplied voltage variation. The much larger

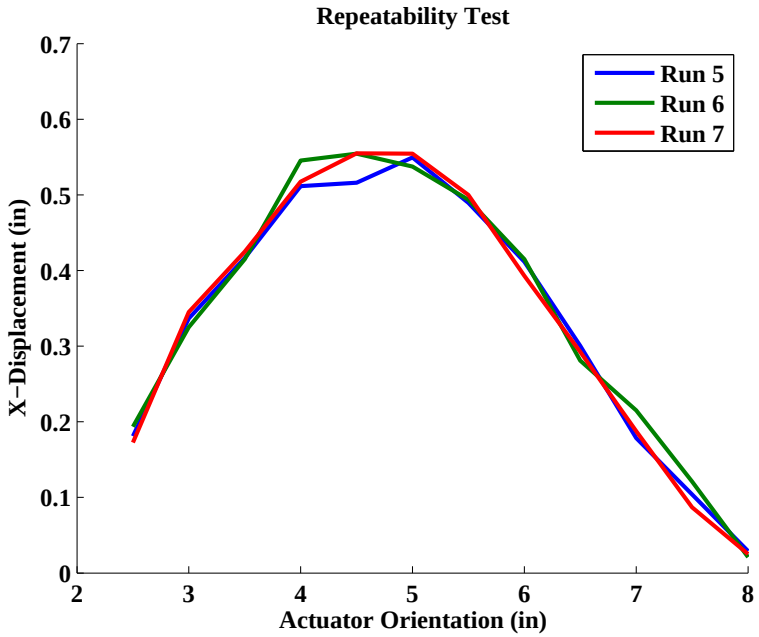

Figure 4.2: The X-displacement measurements are very repeatable for multiple runs of the single-cell experiment.

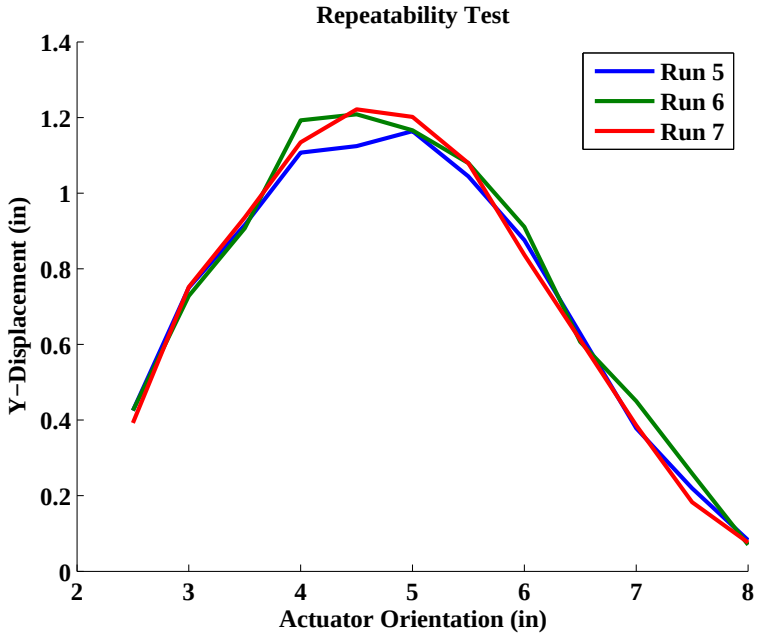

Figure 4.3: The Y-displacement measurements are very repeatable for multiple runs of the single-cell experiment.

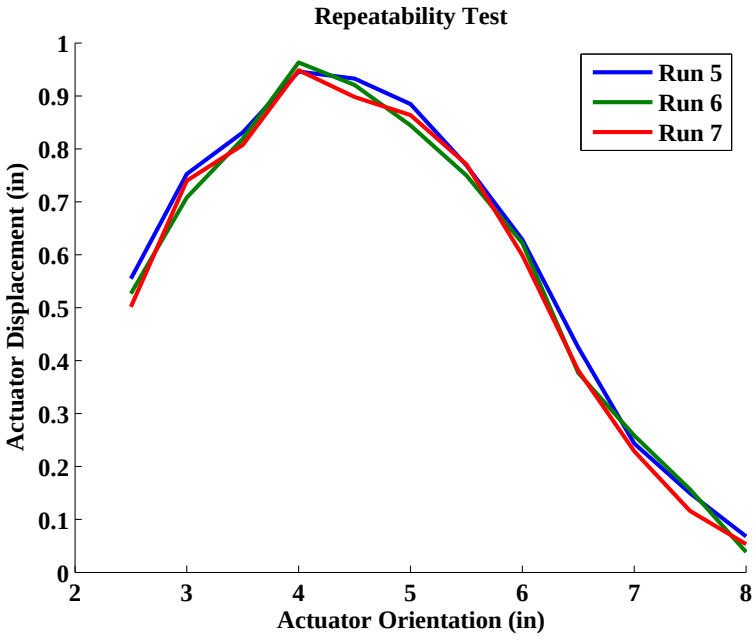

Figure 4.4: The actuator displacement measurements are very repeatable for multiple runs of the single-cell experiment.

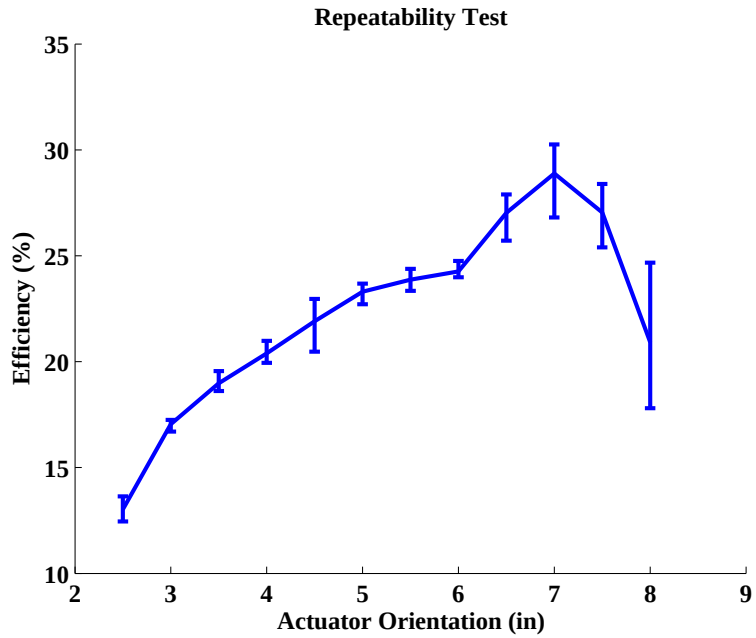

Figure 4.5: The average efficiency for the sing-cell experiment with error bars showing the high and low efficiencies throughout the multiple runs of the experiment.

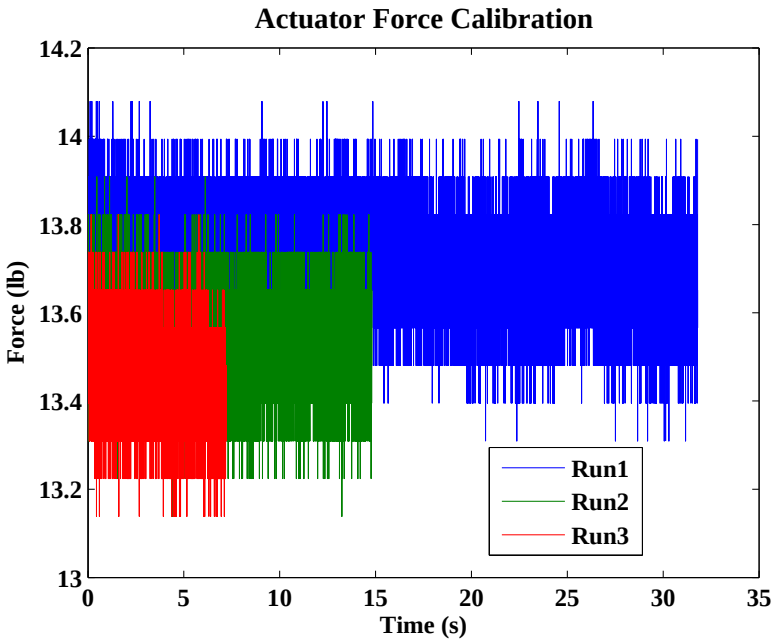

Figure 4.6: The actuator force was measured three times at a sampling rate of 1000 hz.

Table 4.1: Actuator Force Measurements.

Run	Mean Force (lb)	Std Dev
1	13.71	0.1055
2	13.53	0.1022
3	13.45	0.1052
Total	13.6257	0.1470

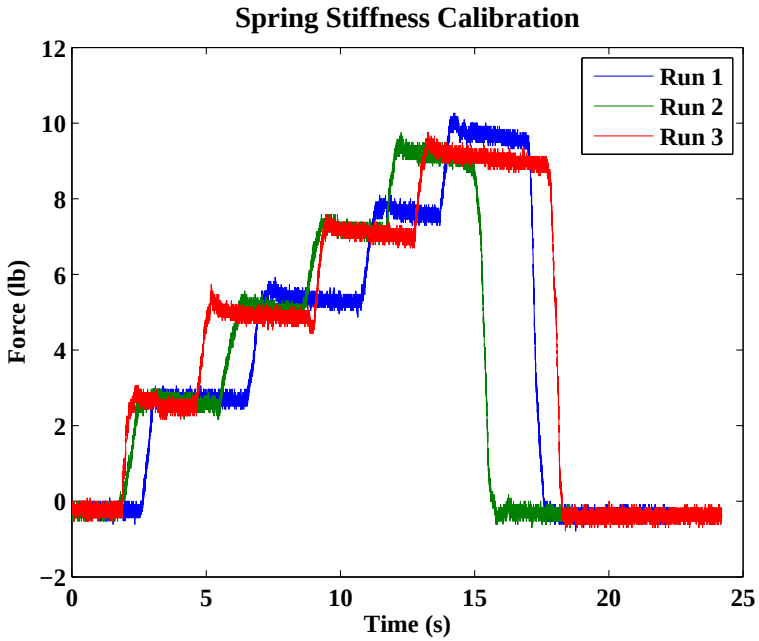

Figure 4.7: Spring Force Displacement Measurements (for 1, 2, 3, and 4 inch displacements).

variation, or shift in mean values, between the three runs is due to the pressure variation. The pressure was continually fluctuating and, while 45.16 psi was the intended supplied air pressure, the pressure varied from around 44.89 to 45.55 psi throughout the tests, according to the pressure transducer readout. The variation in air pressure is approximate as there was no data collection system in place for it, so the variation was merely by observation and no direct correlation to the actuator force could be made. If the air pressure was noticed to stray outside this range during the test, it was adjusted back to within this vicinity of 45.16 psi. The average actuator force was used in the FEM, while the highest and lowest values of actuator force were also used to calculate the error bars for any FEA.

Next, the spring force and material modulus of elasticity were measured in a similar fashion. One end of the spring was held stationary, while the other end was displaced and the force measured. Figure 4.7 shows the resulting forces for displacements of 1, 2, 3, and 4 inches. The x-axis shows the time over which the tests were run. The y-axis shows the force measured.

Table 4.2: The mean resulting spring force and corresponding standard deviation for four different displacements was measured and used to calculate the spring stiffness in the single-cell experiment.

	Run 1		Run 2		Run 3	
Disp (in)	Force (lb)	Std Dev	Force (lb)	Std Dev	Force (lb)	Std Dev
1.0	2.7377	0.1402	2.6340	0.1185	2.5772	0.1571
2.0	5.3860	0.1269	5.1005	0.1189	4.9002	0.1063
3.0	7.6558	0.1396	7.2154	0.1163	7.0823	0.1094
4.0	9.6378	0.1283	9.2021	0.1343	9.0896	0.1375

Table 4.3: The calculated spring stiffness of the single-cell experiment, in lb/in, for each measured force and displacement combination.

Disp (in)	1	2	3	4
Run 1	2.7377	2.6930	2.5519	2.4095
Run 2	2.6340	2.5502	2.4051	2.3005
Run 3	2.5772	2.4501	2.3608	2.2724
Mean	2.6496	2.5644	2.4393	2.3275
Std Dev	0.0664	0.0997	0.0817	0.0591

The data was taken at a sampling rates of 1000 hz, with the mean force and corresponding standard deviation for each displacement shown in Table 4.2. Run 1 shows a shift up in the force, indicating that the displacements were biased for that run. Figure 4.8 shows that this is not a big concern though. The slope of the force-displacement curve in Fig. 4.8 is the measured spring stiffness, and although Figs. 4.7 and 4.8 show a shift in Run 1, the slopes remain consistent.

Table 4.3 shows the calculated spring stiffness for each of the displacements and each run. The average of the three runs is show at the bottom of the table. It also shows that standard deviation is less than 0.1 lb/in for all the measurements. It is important to note that the spring stiffness decreases as the strain increases. This will be discussed later.

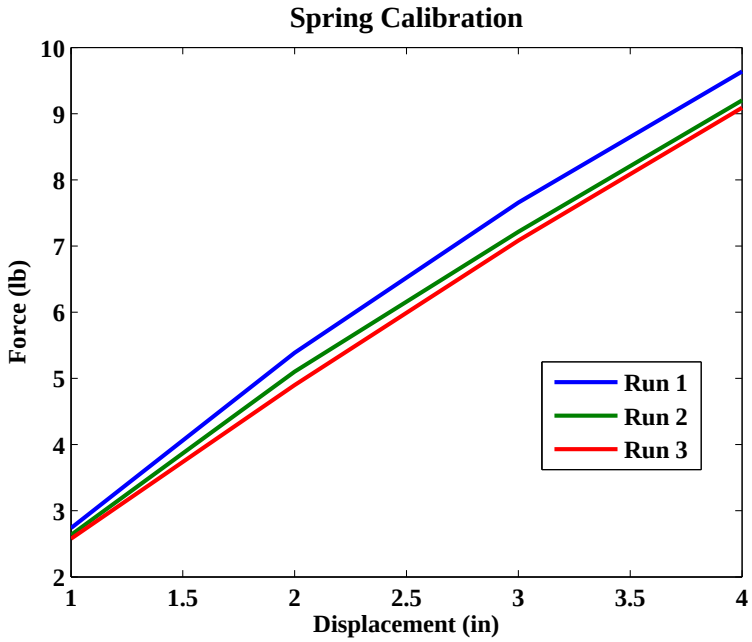

Figure 4.8: Plotting the average force against displacement shows the consistency of the spring stiffness. (force-displacement curve)

The accuracy of the spring stiffness is vital to the accuracy of the FEM. The initial stiffness of the spring was controlled by the cross-sectional area. The spring was modeled as a rod element, and the axial stiffness of a rod element is

$$k_r = \frac{A_e E}{L_e} \tag{4.1}$$

where k_r is the stiffness constant of the rod element, A_e is the cross-sectional area of the element, E is the modulus of elasticity of the material, and L_e is the length of the element. Equation (4.1) also shows that the material modulus of elasticity, E, is essential as well. In a nonlinear analysis using MSC NASTRAN™ the modulus of elasticity for non-linear materials is calculated by using stress-strain data for the material. In a nonlinear solution, the modulus is periodically updated to reflect the value associated with the current strain, so this data needs to be accurate through

Table 4.4: Stress and Strain recalculated from force-displacement measurements.

Stress (psi)	Strain (%)
12.4081	7.0109
24.0184	14.0218
34.2691	21.0328
43.5976	28.0437

the full range of strain experienced by the model. The stress-strain equation,

$$\sigma = E\varepsilon \tag{4.2}$$

where σ is the stress and ε is the strain, shows that the slope of this curve is modulus of elasticity for the material. So, the stress-strain data was calculated from the measured force-displacement data for the spring. The stress was calculated using

$$\sigma = \frac{F}{A_e} \tag{4.3}$$

where F is the measured force at each displacement and A_e was measured to be 0.2135 in^2. The strain was calculated using

$$\varepsilon = \frac{\Delta l_{spring}}{L_e} \tag{4.4}$$

where Δl_{spring} is the measured displacement of the spring and L_e was measured to be 14.235 in. The resulting stress-strain data from these calculations can be seen in Table 4.4. When that resulting data is displayed in Fig. 4.9, it is seen that the stress-strain curve is concave down. This means that the modulus of elasticity of the spring material is getting lower as strain is increasing. This is contrary to the manufacturer's published data on the material properties [1], as seen in Fig. 3.3. This may be because only limited strain was tested. The range of strain tested was only that experienced while running the experiment. The maximum strain tested was

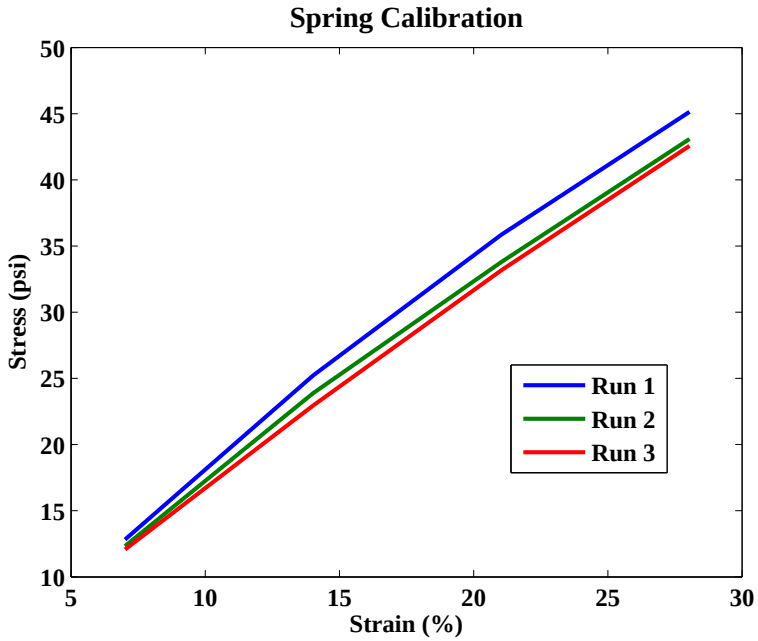

Figure 4.9: Stress and strain data calculated from the measured force and displacements of the spring.

28.04% and the manufacturer only gives one data point at 25% strain and then the next one at 50% strain. Better spring calibration could have possibly resulted from testing higher strains. Although the experiment data shows a slight concave-down trend, it is fairly linear. This shows that material nonlinearity may be negligible for these cases. This is again just because small amounts of strain were tested. The actual N-MAS aircraft has the skin prestressed to lower wrinkling and this was not modeled in the FEM or the experiment. Also, it was assumed that for each configuration the spring initially had zero strain. Besides the pre-straining that was mentioned, this is not a valid assumption. The skin is not reattached at each configuration, so as the wing changes configurations, the skin will be strained in different ways depending on the configuration. So, for the actual aircraft, much larger stains occur during wing morphing, so material nonlinearity may be a factor.

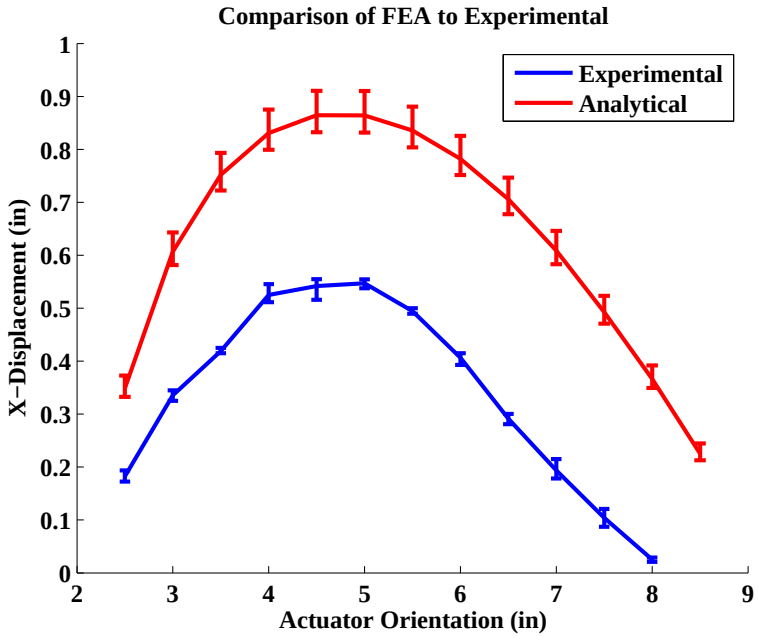

Figure 4.10: Comparison of FEA results to experimental data for one cell [$\theta = 45°$, $F_{act} = 13.625$lbs, $F_x = 3$lbs, and $F_y = 1$lb].

4.2 Comparison of FEM and Experiment

Now that the spring stiffness properties and actuator force properties were measured, those values were used to update the FEM to make it more accurate. A comparison of the FEA data to experimental data was done to verify the accuracy of the FEM. Figures 4.10, 4.11, 4.12, 4.13 show the results of the comparisons for the case where $\theta = 45°$, $F_{act} = 13.625$lbs, $F_x = 3$lbs, and $F_y = 1$lb. In all the figures the x-axis is the actuator orientation, and the y-axis is the measured quantity. The error bars on the experimental data were calculated from the variation of measured data. The error bars on the analytical results were from the variation in actuator force and spring stiffness.

Figures 4.10-4.12 show that the three measured quantities in the experiment, X_{out}, Y_{out}, and Δl_{act} correlate well to the FEA results in regards to the trends, but there is a shift in magnitude. This is not a problem though, because the optimal location and orientation of actuators does not depend on the magnitude of the values,

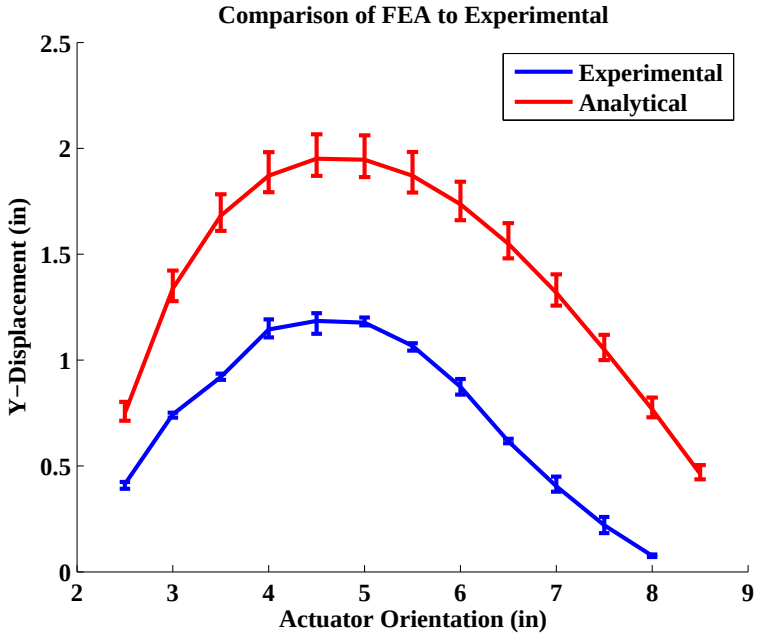

Figure 4.11: Comparison of FEA results to experimental data for one cell [$\theta = 45°$, $F_{act} = 13.625$lbs, $F_x = 3$lbs, and $F_y = 1$lb].

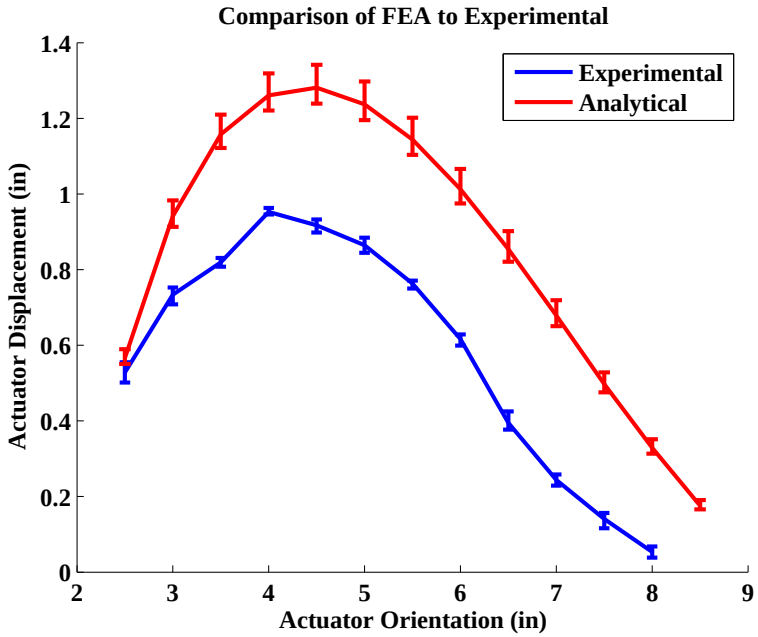

Figure 4.12: Comparison of FEA results to experimental data for one cell [$\theta = 45°$, $F_{act} = 13.625$lbs, $F_x = 3$lbs, and $F_y = 1$lb].

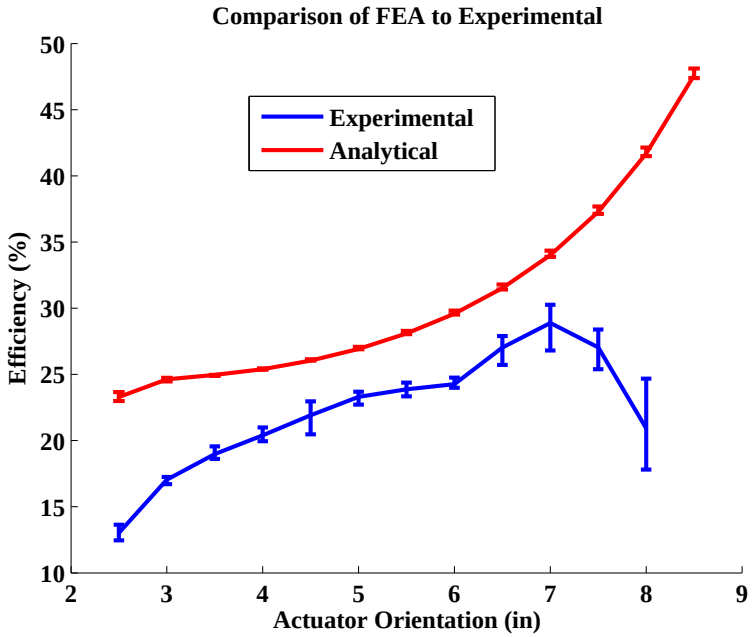

Figure 4.13: Comparison of FEA results to experimental data for one cell [$\theta = 45°$, $F_{act} = 13.625$lbs, $F_x = 3$lbs, and $F_y = 1$lb].

but rather the trends. This begs the question though. Why did the efficiency trends in Fig. 4.13not match well, and isn't this the important quantity for the optimizations? The trends did not match well for the efficiency and this led to an investigation on the efficiency definition.

Figure 4.14 shows the efficiency for both the analytical results and the experimental results. Since the efficiency was defined as a ratio of the work out to the work in, those two values are shown with the efficiency. This shows several interesting things. First, the work output and input trends both correlate well between the analytical and experimental results. The work in is at a maximum around $Z_1 = 4$ for both sets of data. Likewise, the work out is at a maximum around $Z_1 = 5$ for both models. The problem is that the analytical efficiency grows quickly as Z_1 approaches 8.5, whereas the experiment results drop off. This is because the work out for the experimental data is nearly zero, and therefore the efficiency is going to zero as well. Figure 4.14 shows that the work out in the analytical data does not approach zero as

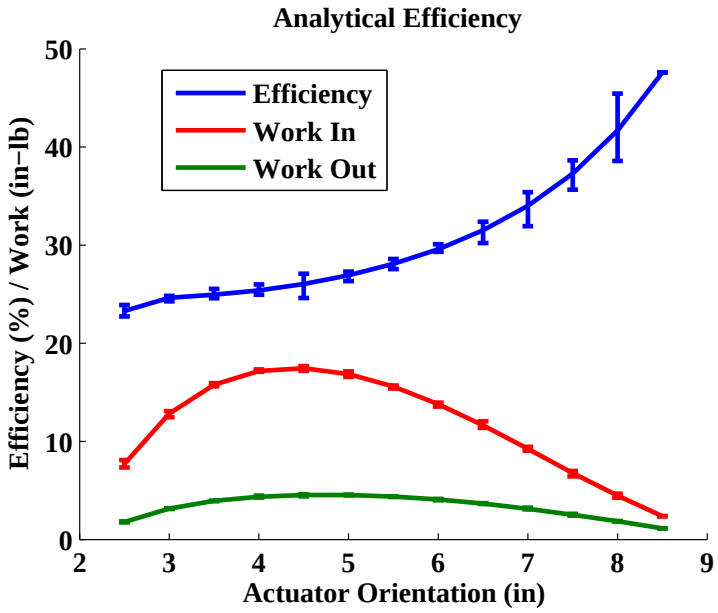

(a)

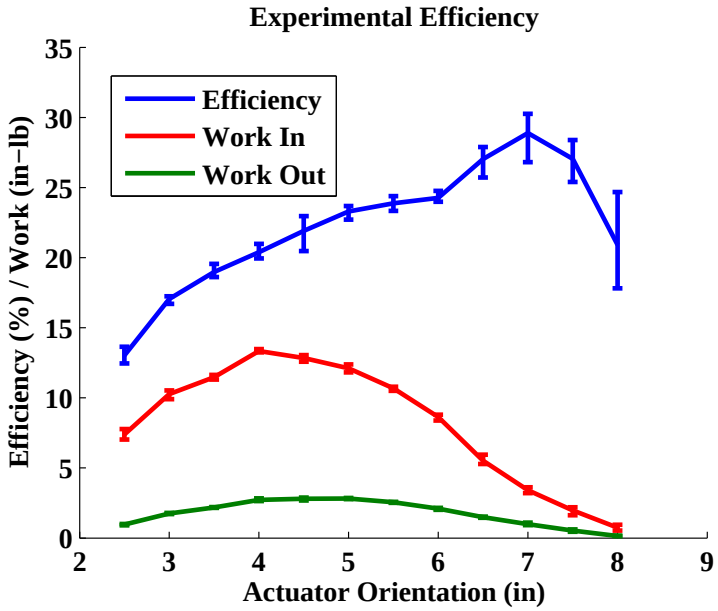

(b)

Figure 4.14: Efficiency, work input, and work output. (a)Analytical (b) Experimental

Table 4.5: Configurations and loading conditions considered in the optimization.

Case Number	θ (degrees)	F_x (lbs)	F_y (lbs)	F_{act} (lbs)
1	45.0	3	3	13.625
2	27.5	3	2	18.0
3	22.4	3	2	20.0
4	15.0	3	1	24.0

quickly. It also shows that experimental efficiency results start to decline when the work in becomes concave up. At this point, the work in slows its approach to zero while the work in is already nearly zero. Efficiency is ill-defined as its numerator and denominator both tend toward zero.

The second lesson drawn from Fig. 4.14 is that assuming the work in is constant and only considering work out is not a valid assumption. This figure clearly shows that the work input is changing. Furthermore, just maximizing the work out would lead to a completely different solution then the current definition. This shows that the definition of efficiency is crucial to the solutions achieved, and the current definition may not be the best choice.

4.3 Optimizations

The experimental results were for a single variable, actuator orientation, being parametrically varied as a single objective, efficiency, was considered. This was done so that he analytical data could be compared to the experimental data to validate the FEM. Now, the accuracy of the optimization results will be examined. It is important that the SQP optimization routine find the actual optimum point in the design space. The cases of varying loading condition and system initial configuration that were considered are given in Table 4.5. For each of the loading conditions and system configurations in Table 4.5 the actuator orientation was parametrically varied while the flexible rib width, and consequently the structural weight, was held constant at 0.125 in. Figure. 4.15 shows that a unique actuator orientation for each case produces

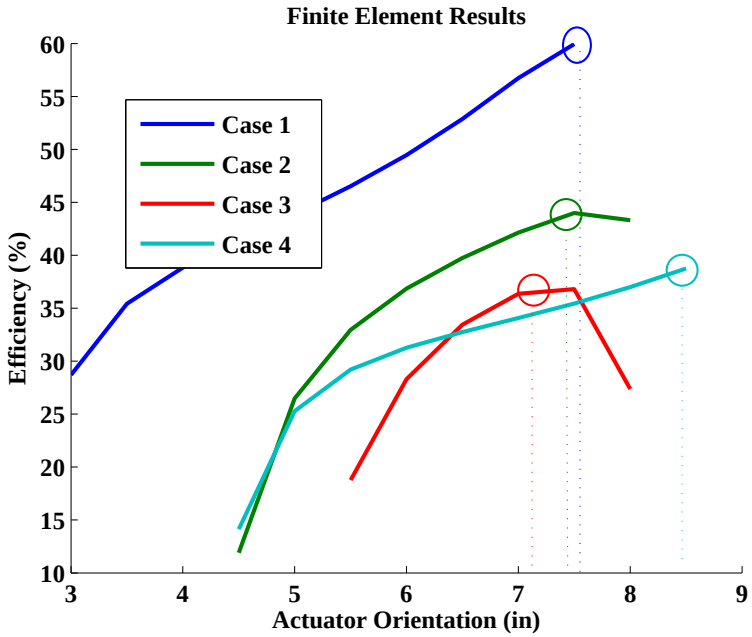

Figure 4.15: Analytical results for parametrically varying design variable. The dotted line shows actuator orientation resulting from optimization.

a maximum efficiency. This is a brute force way of doing a single variable optimization and the results can be used to validate the optimization routine.

Next, optimizations were completed to show that the results coincided with parametrically varying the design variable using FEA. For those optimizations, the rib width was held to a constant 0.125 in. In addition, the weighting factor of the structural weight objective, r_1, was set to zero, while the weighting factor of the efficiency objective, r_2 was set to 1, referring the weighted objective function in Eqn. (1.9). The minimum GA_x and GA_y were set as constraints and set at 0.01 so that they would not be a factor in the optimization. The maximum allowable stress, σ_{max}, was set to the limits of 7075 AL, 67000 psi. The design variable, Z_1 actuator orientation, was allowed to vary from 2 to 8.5 in. The results of each optimization can be seen in Table 4.6. The FEAs done to create Fig. 4.15 were done for 0.5 in increments of Z_1, so because of limited resolution, the exact optimums cannot be found, but the results from Table 4.6 correlate very well with those shown in Fig. 4.15.

Table 4.6: Results of the single variable optimization, with efficiency as the only objective.

Case Number	Z_1 (in)	η (%)	GA_x	GA_y	σ_{max} (psi)
1	7.52	59.98	0.90	1.83	7196
2	7.44	43.82	0.71	2.88	12420
3	7.10	36.70	0.55	2.84	13940
4	8.50	38.75	0.81	6.86	9009

Next, optimizations were done allowing the flexible rib width to be a design variable as well and the structural weight to be an additional objective. First each case number was considered individually, and then all four cases were considered together in the same optimization. For all optimizations the the weighting factor of the structural weight objective, r_1, was set to 15%, while the weighting factor of the efficiency objective, r_2 was set to 85%. These weighting factors were chosen arbitrarily and could be set to any desired value. The weight was also multiplied by a factor of 10 so that it was on the same order of magnitude as the efficiency. For the final optimization where all four cases are considered together, the individual efficiency weighting factors, c_g from Eqn. (1.10), were equal and set to 0.25. The minimum GA_x and GA_y were constrained to be greater than 0.01 so that they would not be a factor in the optimization. The maximum allowable stress, σ_{max}, was set to the limits of 7075 AL, 67000 psi. The design variable, Z_1 actuator orientation, was allowed to vary from 2 to 8.5 in and the rib width, w, was allowed to vary from 0.1 to 1.0 in. The results of all the optimizations can be seen in Table 4.7.

The results show that when each load case and configuration combination is considered separately, the optimal efficiency is higher and the weight lower than when they are considered together. It also shows that the optimal actuator orientation is different for each individual case, and likewise the optimal rib width is different for each case. For a given set of objective weighting factors the optimization over all the combinations of load cases and configurations allows for a unique solution that gives the best efficiency and lowest weight for all uses. Additionally, comparing the results

Table 4.7: Multi-objective optimization results using both rib width and actuator orientation as design variables.

Case Number	1	2	3	4	Combined
actuator orientation (in), Z_1	7.50	4.85	7.69	8.09	7.28
efficiency (%), η	66.64	56.10	57.35	38.77	Table 4.8
rib width (in), w	0.72	1.0	0.42	0.15	0.43
structure weight (lb), W_{struct}	3.45	3.68	3.21	2.99	3.21
GA_x	1.01	0.94	0.90	0.80	0.79
GA_y	2.02	3.64	4.39	6.91	1.98
max stress (psi), σ_{max}	226	305	1091	6697	1148

Table 4.8: These are the efficiencies in each configuration for the final result of the multi-configuration, multi-objective optimization.

Case Number	Efficiency
1	65.18
2	55.85
3	57.07
4	38.56

from Tables 4.7and 4.8 can be to the result in Table 4.6 shows that, in most cases, the additional variable of the rib width, w, not only helps to lower weight, but it also improves over all efficiency. This can be explained by the fact that there is less structural weight, and therefore less gravitational force that the actuator is working against.

4.4 Three-Cell Experiment Scaling

The single-experiment was useful in showing the success of the multi-objective, multi-configuration optimization, and now a larger experiment can be conducted to study the distribution of actuation. The three-cell was designed just for that purpose. More importantly, it was designed so that it is a scaled portion of the N-MAS wind tunnel flutter model. It is scaled to have similar distribution of in-plane stiffness, with minimum manufacturing and assembly difficulties. The optimization set forth in section 3.2.2 resulted in a model design that had a difference of only 0.837% in the non-dimensional displacements and a difference of only 9.72% difference in element strain energies. The exact maximum differences were 2.90e-5 and 2.03e-7 respectively for the non-dimensional displacements and strain energies. With the complexities of the full-scale model removed from the experiment design, the model-matching was quite satisfactory. These results were obtained by allowing the height and width of every scaled member to be a design variable. The end result of varying dimensions from member to member made manufacturability and assembly both costly and difficult. Therefore, another optimization was done where the height of each member was held constant, and only the member widths were allowed to vary. The result was a design that had a maximum non-dimensional displacement difference of 1.08% and non-dimensional strain energy difference of 9.77%. The losses due to only allowing the widths to vary were nominal and therefore those results were used to design three-cell experiment seen in Fig. 4.16. The width of each member influences in-plane bending stiffness to the fourth power while the height only influences in-plane bending stiffness to the first power, so it is no wonder that fixing the height did not change the results

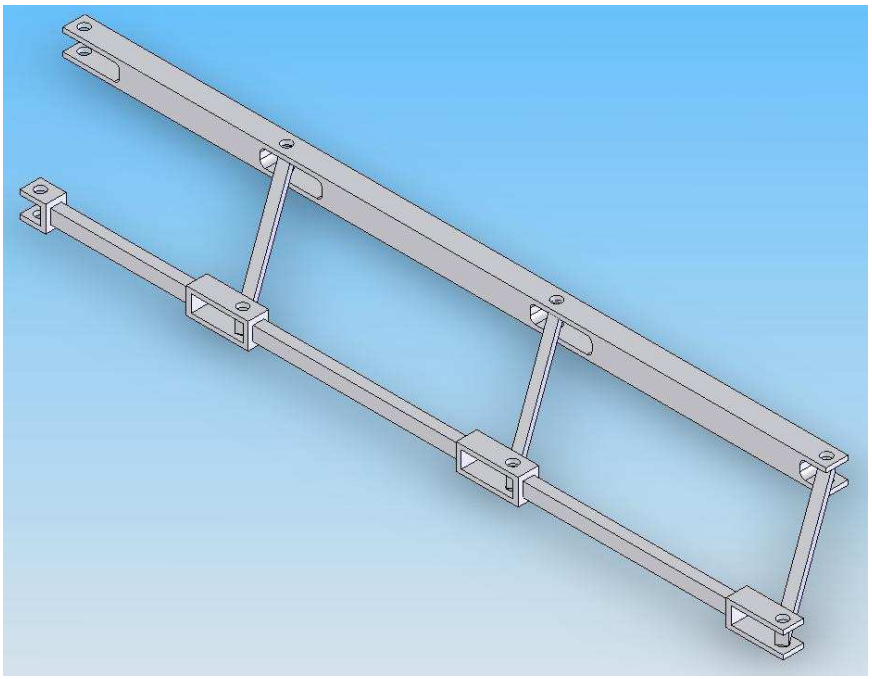

Figure 4.16: The three-cell experiment was designed based on dimensions that were scaled from the N-MAS wind tunnel flutter FEM.

significantly. The three-cell experiment is about 66% the size of the full-model and is designed for a distributed load of about 40% of the approximate full-scale loads. The exact values are not reported because the N-MAS aircraft is proprietary. The dimensions of the experiment can be seen in Table 4.9. The dimensions listed here are the dimensions of the middle portion of each member. The design in Fig. 4.16 shows that these dimensions do not apply near the joints. The joint dimensions had to be adjusted to allow mechanization and assembly.

Table 4.9: These are the final dimensions used to design the three cell experiment.

Link	height (in)	width (in)	length (in)
LE Spar	1.25	1.07	36.0
TE Spar	0.688	0.523	36.0
Rib 1	0.688	0.461	9.82
Rib 2	0.688	0.410	9.82
Rib 3	0.688	0.480	9.82

V. Conclusions and Recommendations

New technology advances in materials and actuators have allowed morphing aircraft to move much closer to being an operational reality. The efficient use of these new technologies is critical to the success of morphing technology. The work done in this research was aimed at making efficient use of those emerging smart materials to make morphing wings feasible on a full-size aircraft. The success of adaptive structures that make morphing wings possible is contingent upon lowering the power requirement to operate them and at the same time lowering the overall weight of those structures. The goal of this research was to set forth a process by which the efficiency could be maximized while the weight is being minimized at the same time.

5.1 Overview

The methods used in developing a process to determine the most efficient and lightest system were both analytical and experimental. The most efficient and lightest system would be designed by determining the optimal location and orientation of a distributed actuation system and at the same time sizing the appropriate structural members. A sequential quadratic programming (SQP) technique written in `Matlab`® was used to do the optimizations. That `Matlab`® script made use of MSC NASTRAN™ to do the nonlinear finite element analysis (FEA), the output of which was used to evaluate the quality of the current design. The optimization routine and the finite element model (FEM) used in the FEA were validated using experimental data collected. With confidence in the optimization routine and FEM, optimizations were then completed beyond the scope of the experimental validation. Additionally, a larger experiment was designed so that it was a scaled portion of a current morphing wing, N-MAS, designed by NextGen Aeronautics. This experiment can be used in conjunction with the developed analytical techniques to make real determinations on the distributed actuation system and sizing of the N-MAS wing. Upon successful completion, the three-cell study can potentially aid in the success of the N-MAS wing being realizable at the full-scale level.

5.2 Conclusions

The data collected with the single cell experiment were very repeatable with the largest variance in measurements being only 5.09%. That resulted in high confidence in the data taken in the single-cell experiment test runs. That data was then used to validate the FEM, which showed the same trends in data with some difference in the magnitude of results. The optimization routines were able to successfully find those optima demonstrated by the experimental results. It was also shown that those optimum orientations of actuators were different for different loading conditions and different geometric configurations of the system. Hence, the necessity of multi-point design considerations, i.e., multiple configurations and loading conditions, was proven. Optimizations were successfully completed that found the optimum actuator orientation and member sizes so that the system would be maximally efficient and have a minimal weight over several configurations and loading conditions. Overall, the optimization process was successful and was validated through experimental results.

A three-cell experiment was designed by scaling a portion of the NextGen N-MAS wind tunnel flutter model. The scaling was very successful, achieving less than 1% difference in non-dimensional displacements and less than 10% difference in non-dimensional strain energies. This experiment can be used in the investigation of actuation distribution. With multiple cells, optimizations can be done to determine which cells should have actuators when the number of actuators available is less than the number of cells.

5.3 Significance of Research

Dr. Kudva said it best,"the optimization of distributed actuation is as an area of research *critical to the success of morphing technology.*" This research can be used to define a formal process by which morphing aircraft, and the adaptive structures that that they are built with, are optimized for weight and efficiency. These are two of the more critical hurdles for morphing aircraft being realizable on the full-scale.

5.4 Recommendations

The definition of efficiency used throughout this research was shown to be lacking and may be made better. Efficiency could be thought of several ways. One option is to find the most efficient actuation distribution so that the actuators can keep the aircraft in a particular configuration. This would mean it would be necessary to minimize the work input, while restricting the displacements, and likewise the work out, to zero. Another option is to look at the efficiency as the wing changes from one configuration to another. This is a transient problem though. As the wing changes shape, the force distribution dynamically changes as well. The efficiency in this case could be defined to minimize the work input required to go from one configuration to another. For simplicity though, the efficiency in this research was defined so that the distribution of actuation maximized the ability to initiate changing shape most efficiently. This is the initial window of the transient problem, but considered to be a static problem for simplification. The efficiency could also be addressed by maximizing the work out and minimizing the work in and treating it as a multi-objective optimization problem. The problem with this is how to weight the importance of each of the objectives. Alternatively, the work in could be thought of as constraint. The work in could be kept constant at some nominal value as a constraint and then the work output could be used as the objective function. This forces the assumption that work input is constant. With this measure of efficiency, the actuator force could also be one of the design variables. Research should be done using these different ways to measure the efficiency of the distributed actuation.

The three-cell experiment should be used in conjunction with a new efficiency definition to investigate the distribution as well as the orientation of actuation. This experiment could be used in the same process used in this research. The results of the three-cell experiment could provide the optimal orientations and locations to place a limited number of actuators throughout the flexible structure. The optimizations to coincide with the experimental results could be used to size the structure to handle in-plane loading conditions. The results of that experiment could be scaled up to directly

relate the the N-MASwing. The scaled up results could estimate weight savings and increased efficiency for the N-MAS aircraft.

Appendix A. DMAP Code

These are the DMAP statements to inlude in the NASTRAN™ input file so that the stiffness matrix is an output of the analysis.

A.1 DMAP Stiffness Output

Listing A.1: DMAP sequence to output stiffness matrix.(appendix1/DMAP.txt)

```
1 $ Use this for global stiffness output
  compile semg
  alter 'kjjz.*stiffness' $
  matpch kjjz// $

6 $ Use this for partitioned stiffness output
  compile sekr $
  alter 'upartn.*kff' $
  matpch kff $
```

Appendix B. Experimental Data

This is the data that was collected when running the single-cell experiment.

B.1 First Run

Table B.1: $\theta = 45°$, $F_{act} = 13.625$lbs, $F_x = 3$lbs, and $F_y = 3$lbs

Z_1 (in)	X_{out} (in)	Y_{out} (in)	Δl_{act} (in)
2.0	0.000	0.000	0.000
2.5	0.452	0.951	0.808
3.0	0.393	0.874	0.770
3.5	0.460	1.008	0.765
4.0	0.457	0.937	0.778
4.5	0.329	0.726	0.510
5.0	0.319	0.697	0.473
5.5	0.290	0.608	0.401
6.0	0.257	0.520	0.313
6.5	0.111	0.222	0.089
7.0	0.004	0.026	-0.041
7.5	0.000	0.000	0.000
8.0	0.000	0.000	0.000
8.5	0.000	0.000	0.000

Table B.2: $\theta = 45°$, $F_{act} = 13.625$lbs, $F_x = 3$lbs, and $F_y = 2$lbs

Z_1 (in)	X_{out} (in)	Y_{out} (in)	Δl_{act} (in)
2.0	0.111	0.161	0.248
2.5	0.611	1.292	0.970
3.0	0.586	1.325	1.023
3.5	0.576	1.294	0.935
4.0	0.647	1.441	1.030
4.5	0.531	1.192	0.800
5.0	0.507	1.121	0.736
5.5	0.477	1.019	0.654
6.0	0.388	0.847	0.508
6.5	0.354	0.770	0.420
7.0	0.202	0.428	0.188
7.5	0.054	0.099	0.017
8.0	0.000	0.000	0.000
8.5	0.000	0.000	0.000

Table B.3: $\theta = 45°$, $F_{act} = 13.625$lbs, $F_x = 3$lbs, and $F_y = 1$lbs

Z_1 (in)	X_{out} (in)	Y_{out} (in)	Δl_{act} (in)
2.0	0.078	0.216	0.267
2.5	0.700	1.547	1.091
3.0	0.709	1.624	1.176
3.5	0.758	1.792	1.205
4.0	0.747	1.667	1.176
4.5	0.691	1.570	1.033
5.0	0.684	1.511	0.970
5.5	0.593	1.281	0.814
6.0	0.627	1.394	0.822
6.5	0.525	1.148	0.628
7.0	0.387	0.831	0.410
7.5	0.219	0.446	0.199
8.0	0.081	0.174	0.004
8.5	0.000	0.000	0.000

Table B.4: $\theta = 45°$, $F_{act} = 13.625$lbs, $F_x = 2$lbs, and $F_y = 3$lbs

Z_1 (in)	X_{out} (in)	Y_{out} (in)	Δl_{act} (in)
2.0	0.000	0.000	0.000
2.5	0.462	0.970	0.813
3.0	0.441	0.973	0.814
3.5	0.520	1.144	0.845
4.0	0.494	1.079	0.833
4.5	0.483	1.060	0.717
5.0	0.473	1.020	0.669
5.5	0.431	0.907	0.592
6.0	0.370	0.791	0.480
6.5	0.329	0.685	0.374
7.0	0.177	0.347	0.143
7.5	0.000	0.000	0.000
8.0	0.000	0.000	0.000
8.5	0.000	0.000	0.000

Table B.5: $\theta = 45°$, $F_{act} = 13.625$lbs, $F_x = 2$lbs, and $F_y = 2$lbs

Z_1 (in)	X_{out} (in)	Y_{out} (in)	Δl_{act} (in)
2.0	0.000	0.000	0.000
2.5	0.613	1.330	0.987
3.0	0.621	1.349	1.012
3.5	0.627	1.384	0.982
4.0	0.683	1.521	1.091
4.5	0.640	1.424	0.941
5.0	0.656	1.430	0.920
5.5	0.573	1.235	0.791
6.0	0.530	1.149	0.688
6.5	0.483	1.045	0.575
7.0	0.362	0.757	0.373
7.5	0.205	0.425	0.191
8.0	0.050	0.110	-0.024
8.5	0.000	0.000	0.000

Table B.6: $\theta = 45°$, $F_{act} = 13.625$lbs, $F_x = 2$lbs, and $F_y = 1$lbs

Z_1 (in)	X_{out} (in)	Y_{out} (in)	Δl_{act} (in)
2.0	0.019	0.093	0.221
2.5	0.782	1.737	1.171
3.0	0.833	1.923	1.317
3.5	0.890	2.024	1.319
4.0	0.858	1.920	1.317
4.5	0.741	1.672	1.087
5.0	0.853	1.877	1.179
5.5	0.818	1.778	1.095
6.0	0.685	1.535	0.899
6.5	0.664	1.463	0.801
7.0	0.435	0.936	0.466
7.5	0.361	0.771	0.366
8.0	0.257	0.536	0.165
8.5	0.067	0.147	-0.025

Table B.7: $\theta = 45°$, $F_{act} = 13.625$lbs, $F_x = 1$lbs, and $F_y = 3$lbs

Z_1 (in)	X_{out} (in)	Y_{out} (in)	Δl_{act} (in)
2.0	0.000	0.000	0.000
2.5	0.456	0.952	0.798
3.0	0.534	1.148	0.921
3.5	0.636	1.420	0.980
4.0	0.580	1.263	0.932
4.5	0.590	1.265	0.845
5.0	0.594	1.273	0.820
5.5	0.560	1.201	0.767
6.0	0.494	1.045	0.625
6.5	0.435	0.894	0.490
7.0	0.329	0.660	0.317
7.5	0.172	0.348	0.159
8.0	0.000	0.000	0.000
8.5	0.000	0.000	0.000

Table B.8: $\theta = 45°$, $F_{act} = 13.625$lbs, $F_x = 1$lbs, and $F_y = 2$lbs

Z_1 (in)	X_{out} (in)	Y_{out} (in)	Δl_{act} (in)
2.0	-0.031	0.034	0.198
2.5	0.650	1.435	1.028
3.0	0.696	1.550	1.117
3.5	0.729	1.629	1.095
4.0	0.782	1.687	1.180
4.5	0.767	1.669	1.079
5.0	0.781	1.748	1.102
5.5	0.737	1.609	1.009
6.0	0.644	1.387	0.821
6.5	0.585	1.272	0.692
7.0	0.483	0.987	0.489
7.5	0.339	0.705	0.337
8.0	0.223	0.444	0.134
8.5	0.008	0.036	-0.066

Table B.9: $\theta = 45°$, $F_{act} = 13.625$lbs, $F_x = 1$lbs, and $F_y = 1$lbs

Z_1 (in)	X_{out} (in)	Y_{out} (in)	Δl_{act} (in)
2.0	0.222	0.499	0.362
2.5	0.767	1.770	1.171
3.0	0.855	1.970	1.333
3.5	0.939	2.138	1.357
4.0	0.944	2.074	1.398
4.5	0.860	1.874	1.197
5.0	0.988	2.196	1.345
5.5	0.997	2.157	1.313
6.0	0.910	2.001	1.145
6.5	0.844	1.785	0.962
7.0	0.658	1.462	0.722
7.5	0.512	1.085	0.516
8.0	0.381	0.789	0.282
8.5	0.245	0.480	0.111

B.2 Second Run

Table B.10: $\theta = 45°$, $F_{act} =$ 13.625lbs, $F_x = 3$lbs, and $F_y = 3$lbs

Z_1 (in)	X_{out} (in)	Y_{out} (in)	Δl_{act} (in)
2.0	0.000	0.000	0.000
2.5	0.000	0.000	0.000
3.0	0.153	0.356	0.603
3.5	0.307	0.657	0.763
4.0	0.298	0.634	0.690
4.5	0.334	0.706	0.696
5.0	0.229	0.497	0.506
5.5	0.252	0.526	0.459
6.0	0.151	0.351	0.322
6.5	0.107	0.236	0.222
7.0	0.000	0.000	0.000
7.5	0.000	0.000	0.000
8.0	0.000	0.000	0.000
8.5	0.000	0.000	0.000

Table B.11: $\theta = 45°$, $F_{act} =$ 13.625lbs, $F_x = 3$lbs, and $F_y = 2$lbs

Z_1 (in)	X_{out} (in)	Y_{out} (in)	Δl_{act} (in)
2.0	0.000	0.000	0.000
2.5	0.082	0.210	0.466
3.0	0.374	0.847	0.889
3.5	0.429	0.963	0.945
4.0	0.477	1.065	0.960
4.5	0.508	1.121	0.957
5.0	0.467	1.025	0.840
5.5	0.410	0.870	0.675
6.0	0.380	0.831	0.614
6.5	0.289	0.612	0.436
7.0	0.134	0.293	0.280
7.5	0.029	0.099	0.222
8.0	0.000	0.000	0.000
8.5	0.000	0.000	0.000

Table B.12: $\theta = 45°$, $F_{act} =$ 13.625lbs, $F_x = 3$lbs, and $F_y = 1$lbs

Z_1 (in)	X_{out} (in)	Y_{out} (in)	Δl_{act} (in)
2.0	0.000	0.000	0.000
2.5	0.270	0.607	0.675
3.0	0.494	1.121	1.034
3.5	0.616	1.383	1.193
4.0	0.647	1.471	1.201
4.5	0.652	1.455	1.153
5.0	0.641	1.420	1.074
5.5	0.597	1.307	0.938
6.0	0.566	1.231	0.843
6.5	0.472	1.019	0.672
7.0	0.326	0.694	0.491
7.5	0.201	0.442	0.417
8.0	-0.021	0.018	0.148
8.5	0.000	0.000	0.000

B.3 Third Run

Table B.13: $\theta = 45°$, $F_{act} =$ 13.625lbs, $F_x = 3$lbs, and $F_y = 3$lbs

Z_1 (in)	X_{out} (in)	Y_{out} (in)	Δl_{act} (in)
2.0	0.000	0.000	0.000
2.5	0.000	0.000	0.000
3.0	0.117	0.265	0.469
3.5	0.206	0.470	0.525
4.0	0.263	0.550	0.549
4.5	0.273	0.565	0.492
5.0	0.168	0.351	0.291
5.5	0.142	0.292	0.219
6.0	0.096	0.235	0.157
6.5	0.030	0.081	0.045
7.0	0.000	0.000	0.000
7.5	0.000	0.000	0.000
8.0	0.000	0.000	0.000
8.5	0.000	0.000	0.000

Table B.14: $\theta = 45°$, $F_{act} =$ 13.625lbs, $F_x = 3$lbs, and $F_y = 2$lbs

Z_1 (in)	X_{out} (in)	Y_{out} (in)	Δl_{act} (in)
2.0	0.000	0.000	0.000
2.5	0.028	0.095	0.267
3.0	0.279	0.585	0.645
3.5	0.381	0.812	0.737
4.0	0.472	0.996	0.831
4.5	0.452	0.955	0.743
5.0	0.415	0.889	0.636
5.5	0.387	0.875	0.542
6.0	0.310	0.631	0.427
6.5	0.236	0.485	0.287
7.0	0.059	0.142	0.174
7.5	0.000	0.000	0.000
8.0	0.000	0.000	0.000
8.5	0.000	0.000	0.000

Table B.15: $\theta = 45°$, $F_{act} =$ 13.625lbs, $F_x = 3$lbs, and $F_y = 1$lbs

Z_1 (in)	X_{out} (in)	Y_{out} (in)	Δl_{act} (in)
2.0	0.000	0.000	0.000
2.5	0.216	0.461	0.463
3.0	0.496	1.091	0.934
3.5	0.573	1.254	1.001
4.0	0.632	1.371	1.053
4.5	0.591	1.295	0.952
5.0	0.595	1.271	0.867
5.5	0.569	1.214	0.793
6.0	0.478	1.016	0.641
6.5	0.415	0.875	0.511
7.0	0.284	0.580	0.403
7.5	0.122	0.264	0.137
8.0	0.000	0.000	0.000
8.5	0.000	0.000	0.000

B.4 Fourth Run

Table B.16: $\theta = 45°$, $F_{act} = 13.625$lbs, $F_x = 3$lbs, and $F_y = 3$lbs

Z_1 (in)	X_{out} (in)	Y_{out} (in)	Δl_{act} (in)
2.0	0.000	0.000	0.000
2.5	0.000	0.000	0.000
3.0	0.121	0.244	0.431
3.5	0.155	0.325	0.427
4.0	0.270	0.547	0.519
4.5	0.333	0.665	0.535
5.0	0.317	0.683	0.567
5.5	0.177	0.401	0.317
6.0	0.155	0.273	0.156
6.5	0.028	0.068	0.026
7.0	0.000	0.000	0.000
7.5	0.000	0.000	0.000
8.0	0.000	0.000	0.000
8.5	0.000	0.000	0.000

Table B.17: $\theta = 45°$, $F_{act} =$ 13.625lbs, $F_x = 3$lbs, and $F_y = 2$lbs

Z_1 (in)	X_{out} (in)	Y_{out} (in)	Δl_{act} (in)
2.0	0.000	0.000	0.000
2.5	-0.006	0.021	0.314
3.0	0.294	0.618	0.646
3.5	0.338	0.698	0.668
4.0	0.462	0.996	0.801
4.5	0.574	1.191	0.871
5.0	0.446	0.954	0.696
5.5	0.376	0.813	0.577
6.0	0.364	0.707	0.419
6.5	0.223	0.440	0.236
7.0	0.167	0.300	0.169
7.5	0.042	0.077	0.024
8.0	0.000	0.000	0.000
8.5	0.000	0.000	0.000

Table B.18: $\theta = 45°$, $F_{act} =$ 13.625lbs, $F_x = 3$lbs, and $F_y = 1$lbs

Z_1 (in)	X_{out} (in)	Y_{out} (in)	Δl_{act} (in)
2.0	0.000	0.000	0.000
2.5	0.212	0.459	0.550
3.0	0.462	1.002	0.861
3.5	0.542	1.046	0.888
4.0	0.646	1.428	1.057
4.5	0.653	1.408	1.011
5.0	0.623	1.354	0.939
5.5	0.547	1.197	0.804
6.0	0.529	1.077	0.640
6.5	0.407	0.823	0.450
7.0	0.374	0.742	0.400
7.5	0.206	0.381	0.181
8.0	0.084	0.153	0.069
8.5	0.000	0.000	0.000

Table B.19: $\theta = 45°$, $F_{act} =$ 13.625lbs, $F_x = 2$lbs, and $F_y = 3$lbs

Z_1 (in)	X_{out} (in)	Y_{out} (in)	Δl_{act} (in)
2.0	0.000	0.000	0.000
2.5	0.012	0.046	0.329
3.0	0.252	0.536	0.615
3.5	0.345	0.712	0.683
4.0	0.427	0.873	0.729
4.5	0.496	1.008	0.760
5.0	0.421	0.861	0.639
5.5	0.392	0.843	0.597
6.0	0.281	0.527	0.315
6.5	0.214	0.412	0.218
7.0	0.152	0.267	0.149
7.5	0.000	0.000	0.000
8.0	0.000	0.000	0.000
8.5	0.000	0.000	0.000

Table B.20: $\theta = 45°$, $F_{act} =$ 13.625lbs, $F_x = 2$lbs, and $F_y = 2$lbs

Z_1 (in)	X_{out} (in)	Y_{out} (in)	Δl_{act} (in)
2.0	0.000	0.000	0.000
2.5	0.229	0.484	0.569
3.0	0.429	0.888	0.806
3.5	0.535	1.135	0.948
4.0	0.607	1.299	0.978
4.5	0.648	1.355	0.974
5.0	0.583	1.242	0.874
5.5	0.586	1.257	0.847
6.0	0.485	0.972	0.576
6.5	0.403	0.795	0.436
7.0	0.314	0.612	0.333
7.5	0.207	0.381	0.179
8.0	0.056	0.092	0.046
8.5	0.000	0.000	0.000

Table B.21: $\theta = 45°$, $F_{act} =$ 13.625lbs, $F_x = 2$lbs, and $F_y = 1$lbs

Z_1 (in)	X_{out} (in)	Y_{out} (in)	Δl_{act} (in)
2.0	0.000	0.000	0.000
2.5	0.402	0.861	0.746
3.0	0.613	1.305	1.029
3.5	0.739	1.604	1.210
4.0	0.743	1.651	1.178
4.5	0.771	1.713	1.184
5.0	0.756	1.655	1.120
5.5	0.712	1.561	1.051
6.0	0.664	1.375	0.802
6.5	0.620	1.272	0.688
7.0	0.496	1.005	0.543
7.5	0.353	0.693	0.332
8.0	0.230	0.447	0.200
8.5	0.054	0.087	0.111

Table B.22: $\theta = 45°$, $F_{act} =$ 13.625lbs, $F_x = 1$lbs, and $F_y = 3$lbs

Z_1 (in)	X_{out} (in)	Y_{out} (in)	Δl_{act} (in)
2.0	0.000	0.000	0.000
2.5	0.216	0.418	0.538
3.0	0.395	0.781	0.737
3.5	0.520	1.053	0.888
4.0	0.550	1.109	0.865
4.5	0.555	1.133	0.827
5.0	0.543	1.143	0.815
5.5	0.472	0.985	0.653
6.0	0.413	0.814	0.482
6.5	0.380	0.736	0.397
7.0	0.284	0.551	0.305
7.5	0.169	0.190	0.294
8.0	0.000	0.000	0.000
8.5	0.000	0.000	0.000

Table B.23: $\theta = 45°$, $F_{act} =$ 13.625lbs, $F_x = 1$lbs, and $F_y = 2$lbs

Z_1 (in)	X_{out} (in)	Y_{out} (in)	Δl_{act} (in)
2.0	0.000	0.000	0.000
2.5	0.384	0.762	0.708
3.0	0.542	1.125	0.930
3.5	0.667	1.416	1.096
4.0	0.723	1.559	1.124
4.5	0.716	1.587	1.113
5.0	0.737	1.592	1.077
5.5	0.638	1.386	0.898
6.0	0.590	1.216	0.711
6.5	0.527	1.066	0.575
7.0	0.443	0.880	0.473
7.5	0.358	0.701	0.549
8.0	0.200	0.370	0.164
8.5	0.016	0.021	0.102

Table B.24: $\theta = 45°$, $F_{act} =$ 13.625lbs, $F_x = 1$lbs, and $F_y = 1$lbs

Z_1 (in)	X_{out} (in)	Y_{out} (in)	Δl_{act} (in)
2.0	0.073	0.113	0.236
2.5	0.563	1.149	0.895
3.0	0.707	1.511	1.138
3.5	0.876	1.857	1.343
4.0	0.873	1.924	1.331
4.5	0.926	2.055	1.377
5.0	0.921	2.031	1.323
5.5	0.872	1.931	1.201
6.0	0.802	1.716	0.989
6.5	0.730	1.534	0.818
7.0	0.641	1.307	0.690
7.5	0.522	1.060	0.716
8.0	0.376	0.731	0.316
8.5	0.228	0.434	0.262

B.5 Fifth Run

Table B.25: $\theta = 45°$, $F_{act} = 13.625$lbs, $F_x = 3$lbs, and $F_y = 3$lbs

Z_1 (in)	X_{out} (in)	Y_{out} (in)	Δl_{act} (in)
2.0	0.000	0.000	0.000
2.5	0.009	0.049	0.350
3.0	0.102	0.255	0.475
3.5	0.165	0.368	0.496
4.0	0.204	0.442	0.534
4.5	0.197	0.422	0.463
5.0	0.186	0.394	0.396
5.5	0.144	0.315	0.302
6.0	0.084	0.180	0.199
6.5	0.000	0.000	0.000
7.0	0.000	0.000	0.000
7.5	0.000	0.000	0.000
8.0	0.000	0.000	0.000
8.5	0.000	0.000	0.000

Table B.26: $\theta = 45°$, $F_{act} =$ 13.625lbs, $F_x = 3$lbs, and $F_y = 2$lbs

Z_1 (in)	X_{out} (in)	Y_{out} (in)	Δl_{act} (in)
2.0	0.000	0.000	0.000
2.5	0.088	0.243	0.460
3.0	0.200	0.465	0.592
3.5	0.261	0.594	0.634
4.0	0.349	0.752	0.718
4.5	0.359	0.776	0.692
5.0	0.349	0.749	0.630
5.5	0.298	0.630	0.505
6.0	0.227	0.466	0.376
6.5	0.143	0.302	0.230
7.0	0.052	0.117	0.101
7.5	0.000	0.000	0.000
8.0	0.000	0.000	0.000
8.5	0.000	0.000	0.000

Table B.27: $\theta = 45°$, $F_{act} =$ 13.625lbs, $F_x = 3$lbs, and $F_y = 1$lbs

Z_1 (in)	X_{out} (in)	Y_{out} (in)	Δl_{act} (in)
2.0	0.000	0.000	0.000
2.5	0.181	0.425	0.555
3.0	0.337	0.750	0.753
3.5	0.416	0.916	0.831
4.0	0.512	1.107	0.946
4.5	0.516	1.125	0.932
5.0	0.549	1.164	0.884
5.5	0.490	1.045	0.769
6.0	0.411	0.876	0.629
6.5	0.300	0.628	0.425
7.0	0.179	0.379	0.243
7.5	0.104	0.220	0.149
8.0	0.029	0.083	0.068
8.5	0.000	0.000	0.000

B.6 Sith Run

Table B.28: $\theta = 45°$, $F_{act} =$ 13.625lbs, $F_x = 3$lbs, and $F_y = 3$lbs

Z_1 (in)	X_{out} (in)	Y_{out} (in)	Δl_{act} (in)
2.0	0.000	0.000	0.000
2.5	0.000	0.000	0.000
3.0	0.088	0.211	0.402
3.5	0.116	0.274	0.427
4.0	0.185	0.406	0.471
4.5	0.185	0.396	0.400
5.0	0.175	0.398	0.377
5.5	0.137	0.289	0.260
6.0	0.083	0.190	0.198
6.5	0.000	0.000	0.000
7.0	0.000	0.000	0.000
7.5	0.000	0.000	0.000
8.0	0.000	0.000	0.000
8.5	0.000	0.000	0.000

Table B.29: $\theta = 45°$, $F_{act} =$ 13.625lbs, $F_x = 3$lbs, and $F_y = 2$lbs

Z_1 (in)	X_{out} (in)	Y_{out} (in)	Δl_{act} (in)
2.0	0.000	0.000	0.000
2.5	0.071	0.187	0.406
3.0	0.189	0.446	0.546
3.5	0.263	0.581	0.624
4.0	0.377	0.801	0.723
4.5	0.368	0.780	0.647
5.0	0.361	0.762	0.599
5.5	0.311	0.662	0.498
6.0	0.239	0.505	0.400
6.5	0.157	0.333	0.225
7.0	0.079	0.170	0.108
7.5	0.000	0.000	0.000
8.0	0.000	0.000	0.000
8.5	0.000	0.000	0.000

Table B.30: $\theta = 45°$, $F_{act} =$ 13.625lbs, $F_x = 3$lbs, and $F_y = 1$lbs

Z_1 (in)	X_{out} (in)	Y_{out} (in)	Δl_{act} (in)
2.0	0.000	0.000	0.000
2.5	0.194	0.425	0.526
3.0	0.325	0.728	0.708
3.5	0.415	0.907	0.819
4.0	0.546	1.192	0.963
4.5	0.555	1.208	0.921
5.0	0.538	1.166	0.845
5.5	0.494	1.079	0.750
6.0	0.415	0.911	0.622
6.5	0.281	0.607	0.377
7.0	0.215	0.450	0.259
7.5	0.121	0.259	0.157
8.0	0.021	0.070	0.038
8.5	0.000	0.000	0.000

B.7 Seventh Run

Table B.31: $\theta = 45°$, $F_{act} = 13.625$lbs, $F_x = 3$lbs, and $F_y = 3$lbs

Z_1 (in)	X_{out} (in)	Y_{out} (in)	Δl_{act} (in)
2.0	0.000	0.000	0.000
2.5	0.000	0.000	0.000
3.0	0.082	0.215	0.424
3.5	0.149	0.328	0.442
4.0	0.165	0.352	0.461
4.5	0.137	0.307	0.327
5.0	0.180	0.381	0.358
5.5	0.122	0.257	0.254
6.0	0.078	0.155	0.189
6.5	0.000	0.000	0.000
7.0	0.000	0.000	0.000
7.5	0.000	0.000	0.000
8.0	0.000	0.000	0.000
8.5	0.000	0.000	0.000

Table B.32: $\theta = 45°$, $F_{act} =$ 13.625lbs, $F_x = 3$lbs, and $F_y = 2$lbs

Z_1 (in)	X_{out} (in)	Y_{out} (in)	Δl_{act} (in)
2.0	0.000	0.000	0.000
2.5	0.072	0.196	0.399
3.0	0.192	0.421	0.545
3.5	0.276	0.595	0.613
4.0	0.334	0.728	0.731
4.5	0.341	0.748	0.610
5.0	0.364	0.758	0.596
5.5	0.293	0.621	0.490
6.0	0.258	0.538	0.426
6.5	0.124	0.257	0.169
7.0	0.034	0.068	0.050
7.5	0.000	0.000	0.000
8.0	0.000	0.000	0.000
8.5	0.000	0.000	0.000

Table B.33: $\theta = 45°$, $F_{act} =$ 13.625lbs, $F_x = 3$lbs, and $F_y = 1$lbs

Z_1 (in)	X_{out} (in)	Y_{out} (in)	Δl_{act} (in)
2.0	0.000	0.000	0.000
2.5	0.172	0.393	0.501
3.0	0.345	0.752	0.740
3.5	0.425	0.936	0.807
4.0	0.517	1.135	0.948
4.5	0.555	1.222	0.898
5.0	0.554	1.202	0.864
5.5	0.500	1.079	0.771
6.0	0.393	0.837	0.599
6.5	0.292	0.613	0.382
7.0	0.188	0.386	0.229
7.5	0.087	0.183	0.116
8.0	0.025	0.076	0.053
8.5	0.000	0.000	0.000

Bibliography

1. "Torr Technologies Silicone Rubber Sheeting". URL `http://www.torrtech.com/Pages/Silicone-Sheet.htm`.

2. Andersen, Gerald R., David L. Cowan, and David J. Piatak. "Aeroelastic Modeling, Analysis and Testing of a Morphing Wing Structure". *48th AIAA/ASME/ASCE/AHS/ASC Structures, Structural Dynamics, and Materials Conference*. 23-26 April 2007.

3. Bartley-Cho, Jonathan D., Donny P. Wang, and Jayanth N. Kudva. "Shape Estimation of Deforming Structures". *42nd AIAA/ASME/ASCE/AHS/ASC Structures, Structural Dynamics, and Materials Conference*. 16-19 April 2001.

4. Baycan, C. M., S. Utku, S. K. Das, and B. K. Wada. "Optimal Actuator Placement in Adaptive Precision Trusses". *33rd AIAA/ASME/ASCE/AHS/ASC Structures, Structural Dynamics and Materials Conference*, 418–423. 13-15 April 1992.

5. Bisplinghoff, Raymond L., Holt Ashley, and Robert L. Halfman. *Aeroelasticity*. Dover Publications, New York, 1996. ISBN 0486691896. Raymond L. Bisplinghoff, Holt Ashley, Robert L. Halfman.; Corrected republication of the work originally published: Cambridge, Mass. : Addison-Wesley, 1955.; Includes bibliographical references (p. 827-849) and indexes.

6. Bowman, Jason, Brian Sanders, Bryan Cannon, Jayanth Kudva, Shiv Joshi, and Terrence Weisshaar. "Development of Next Generation Morphing Aircraft Structures". *48th AIAA/ASME/ASCE/AHS/ASC Structures, Structural Dynamics, and Materials Conference*. 23-26 April 2007.

7. Bowman, Jason, Brian Sanders, and Terrence Weisshaar. "Evaluating the Impact of Morphing Technologies on Aircraft Performance". *43rd AIAA/ASME/ASCE/AHS/ASC Structures, Structural DynamicS and Materials Conference*. 22-25 April 2002.

8. Bowman, Jason, Brian P. Sanders, and Terrence A. Weisshaar. "Identification of military morphing aircraft missions and morphing technology assessment". volume 4698, 121–132. SPIE, July 9, 2002 2002.

9. Burden, Richard L. and J. Douglas Faires. *Numerical analysis*. Thomson Brooks/Cole, Australia, Belmont, CA, 2005. ISBN 0534392008. Richard L. Burden, J. Douglas Faires.; Includes bibliographical references (p. 747-746) and index.

10. Colbrunn, R. W., G. M. Nelson, and R. D. Quinn. "Modeling of Braided Pneumatic Actuators for Robotic Control". *International Conference on Intelligent Robots and Systems*, volume 4, 1964–1970. 10/29/2001 - 11/03/2001 2001. ISBN 0-7803-6612-3.

11. Flanagan, John S., Rolf C. Strutzenberg, Robert B. Myers, and Jeffery E. Rodrian. "Development and Flight Testing of a Morphing Aircraft, the NextGen MFX-1". *48th AIAA/ASME/ASCE/AHS/ASC Structures, Structural Dynamics, and Materials Conference*. 23-26 April 2007.

12. French, Mark and F. E. Eastep. "Aeroelastic Model Design Using Parameter Identification". *Journal of Aircraft*, 33(1):198–202, 1996.

13. Gandhi, Neha, Akhilesh Jha, Jeffery Monaco, Thomas Michael Seigler, David Ward, and David J. Inman. "Intelligent Control of a Morphing Aircraft". *48th AIAA/ASME/ASCE/AHS/ASC Structures, Structural Dynamics, and Materials Conference*. 23-26 April 2007.

14. Gern, Frank H., Daniel J. Inman, and Rakesh K. Kapania. "Structural and Aeroelastic Modeling of General Planform UCAV Wings with Morphing Airfoils". *42nd AIAA/ASME/ASCE/AHS/ASC Structures, Structural DynamicS and Materials Conference*. 16-19 April 2001.

15. Hendersen, Joseph A. "Global Optimization Methods for Aeroservoelastic Concepts". *43rd AIAA/ASME/ASCE/AHS/ASC Structures, Structural DynamicS and Materials Conference*. 22-25 April 2002.

16. Hodges, Dewey H. and G. Alvin Pierce. *Introduction to structural dynamics and aeroelasticity*, volume 15. Cambridge University Press, Cambridge, England ; New York, 2002. ISBN 0521806984. Dewey H. Hodges, G. Alvin Pierce.; Includes bibliographical references (p. 164-165) and index.

17. Inoyama, Daisaku, Brian P. Sanders, and James J. Joo. "Conceptual design and multidisciplinary optimization of in-plane morphing wing structures". Lindner D. K. (editor), *Smart Structures and Materials 2006: Modeling, Signal Processing, and Control. Edited by Lindner, Douglas K. Proceedings of the SPIE, Volume 6166, pp. 1-11 (2006).; Presented at the Society of Photo-Optical Instrumentation Engineers (SPIE) Conference*, volume 6166, 1–11. apr 2006.

18. Joo, James J., Brian Sanders, Terrence Johnson, and Mary I. Frecker. "Optimal actuator location within a morphing wing scissor mechanism configuration". volume 6166, 616603. SPIE, March 16, 2006 2006.

19. Joo, James J., Brian Sanders, and Gregory Washington. "Energy based efficiency of adaptive structure systems". *Smart Materials and Structures*, 15(1):171–181, 2006.

20. Kudva, Jayanth N., Kari Appa, Christopher A. Martin, A. Peter Jardine, George Sendeckyj, Terry Harris, Anna-Marie McGowan, and Renee Lake. "Design, Fabrication, and Testing of the DARPA / Wright Lab Smart Wing Wing Tunnel Model". *38th AIAA/ASME/ASCE/AHS/ASC Structures, Structural Dynamics, and Materials Conference and Exhibit*. 7-10 April 1997.

21. Maute, K. and G. W. Reich. "An Aeroelastic Topology Optimization Approach for Adaptive Wing Design". *45th AIAA/ASME/ASCE/AHS/ASC Structures, Structural DynamicS and Materials Conference*. 19-22 April 2004.

22. Perkins, David A., John L. Reed, and Ernie Havens. "Morphing Wing Structures for Loitering Air Vehicles". *45th AIAA/ASME/ASCE/AHS/ASC Structures, Structural Dynamics, and Materials Conference*. 19-22 April 2004.

23. Prock, Brian C., Terrence A. Weisshaar, and William A. Crossley. "Morphing Airfoil Shape Change Optimization with Minimum Actuator Energy as an Objective". *9th AIAA/ISSMO Symposium on Multidisciplinary Analysis and Optimization*. 4-6 September 2002.

24. Raymer, Daniel P. *Aircraft design : a conceptual approach*. American Institute of Aeronautics and Astronautics, Reston, Va., 2006. ISBN 1563478293; 1563478307. 9781563478291; Daniel P. Raymer.; Includes bibliographical references (p. 817-823) and index.

25. Schittkowski, Klaus. *Nonlinear programming codes : information, tests, performance*, volume 183. Springer-Verlag, Berlin ; New York, 1980. ISBN 0387102477. Klaus Schittkowski.; 8009.; Bibliography: p. [174]-190.; Lecture notes in economics and mathematical systems, 183.

26. Skillen, Michael D. and William A. Crossley. "Developing Morphing Wing Weight Predictors with Emphasis on the Actuating Mechanism". *47th AIAA/ASME/ASCE/AHS/ASC Structures, Structural Dynamics, and Materials Conference*. 1-4 May 2006.

27. Summers, Adam. "Biomechanics", 2001.

28. Toensmeier, Patrick A. "Radical Departure". *Aviation Week and Space Technology*, 162(21):72, May 23 2005.

Vita

James Westfall was born in Austin Texas, but lived most of his life in the Cleveland Ohio area. He graduated from North Royalton High School in 1997. He went on to earn a Bachelors degree in Mechanical Engineering from University of Dayton in 2002. He was also received a reserve commission through the ROTC program at Wright State University Detachment 643. His first assignment was at Robins AFB, Georgia as an aircraft maintenance officer for the 93rd Air Control Wing, which after a few months of being there merged with the Georgia ANG 116th Bomb Wing to become the first Total Force wing named the 116th Air Control Wing. During his time as an aircraft maintenance officer James participated in many exercises including Air Warrior and Red Flag, but the highlight of this assignment was deploying to Al Udeid Air Base in Qatar for Operations Iraqi Freedom and Enduring Freedom in the summer of 2004. Then in the fall of 2005 he began attending Air Force Institute of Technology at Wright-Patterson AFB, Ohio in pursuit of a Masters degree in Aeronautical Engineering. Upon completion in June of 2007 he will be going to work at the Air Force Research Laboratory Air Vehicle Directorate at Wright-Patterson AFB, Ohio.

Permanent address: 2950 Hobson Way
Air Force Institute of Technology
Wright-Patterson AFB, OH 45433

Index

The index is conceptual and does not designate every occurrence of a keyword. Page numbers in bold represent concept definition or introduction.

AFW, 15

Code Listings
  appendix1/DMAP.txt, 69
COTS, 7

DARPA, 16
DMC, 17
DMF, 17
dof, 4

FEA, 10
FEM, 10
FEMAP, 11

GA, 7

MAW, 15
MXF-1, 18

N-MAS, 3

SMA, 16
SMP, 17
SQP, 10, 25

UAV, 11

REPORT DOCUMENTATION PAGE

Form Approved
OMB No. 074-0188

The public reporting burden for this collection of information is estimated to average 1 hour per response, including the time for reviewing instructions, searching existing data sources, gathering and maintaining the data needed, and completing and reviewing the collection of information. Send comments regarding this burden estimate or any other aspect of the collection of information, including suggestions for reducing this burden to Department of Defense, Washington Headquarters Services, Directorate for Information Operations and Reports (0704-0188), 1215 Jefferson Davis Highway, Suite 1204, Arlington, VA 22202-4302. Respondents should be aware that notwithstanding any other provision of law, no person shall be subject to an penalty for failing to comply with a collection of information if it does not display a currently valid OMB control number.
PLEASE DO NOT RETURN YOUR FORM TO THE ABOVE ADDRESS.

1. REPORT DATE *(DD-MM-YYYY)*	**2. REPORT TYPE**	**3. DATES COVERED** *(From – To)*
14 Jun 07	**Master's Thesis**	**Jan 2006 – Jun 2007**

4. TITLE AND SUBTITLE

Structural Optimization of a Distributed Actuation System in a Flexible In-Plane Morphing Wing

5a. CONTRACT NUMBER

5b. GRANT NUMBER

5c. PROGRAM ELEMENT NUMBER

6. AUTHOR(S)

Westfall, James T., Captain, USAF

5d. PROJECT NUMBER

5e. TASK NUMBER

5f. WORK UNIT NUMBER

7. PERFORMING ORGANIZATION NAMES(S) AND ADDRESS(S)
Air Force Institute of Technology
Graduate School of Engineering and Management (AFIT/EN)
2950 Hobson Way
WPAFB OH 45433-7765

8. PERFORMING ORGANIZATION REPORT NUMBER

AFIT/GAE/ENY/07-J22

9. SPONSORING/MONITORING AGENCY NAME(S) AND ADDRESS(ES)
AFRL/VASA
Attn: Dr. Brian Sanders
2210 8th St. B146 R219
WPAFB OH 45433 DSN: 785-8296

10. SPONSOR/MONITOR'S ACRONYM(S)

11. SPONSOR/MONITOR'S REPORT NUMBER(S)

12. DISTRIBUTION/AVAILABILITY STATEMENT
APPROVED FOR PUBLIC RELEASE; DISTRIBUTION UNLIMITED.

13. SUPPLEMENTARY NOTES

14. ABSTRACT

Structural weight and efficiency are two major hurdles for morphing aircraft being realizable on the full-scale level, both of which are addressed in this research. The optimal distribution and orientation of actuators throughout an in-plane flexible morphing wing structure is investigated. The drive to minimize structural weight causes a wing to be more flexible and the location and orientation of the actuators become more critical as the structure becomes more flexible. NextGen's N-MAS morphing wing is used as a case study. The wing is modeled as a number of unit cells assembled in a scissor-like structure, each comprised of four linkages pinned together and an actuator. The flexible skin of the wing is modeled with a nonlinear material stretched between two opposing vertices. It will be shown that the optimal orientation of the actuators will vary depending on the loading conditions and initial configuration of the wing. Sequential quadratic programming (SQP) optimization techniques are utilized to orient those actuators and effectively size the members of the structure. The goal is to minimize weight while maximizing the geometric advantage and efficiency. The constraints are member stresses and the force transferred to the actuators is not to be greater than the force the actuator is able to produce. Matlab code is developed to do the SQP optimization while NASTRAN is utilized to do the nonlinear finite element analysis required to evaluate the objective function and constraints. The single-cell results are compared to experimental data to validate the finite element model and optimization routine. A three-cell experiment is designed by utilizing aeroelastic scaling techniques. Matlab is used to develop the scaling problem while the actual scaling is done as an optimization in NASTRAN. The objective for scaling the wing is to minimize the differences in the non-dimensional displacements and strain energies between the two models, using the element cross-sectional dimensions as design variables.

15. SUBJECT TERMS
Structural Optimization, Distributed Actuation, Morphing Wing, Aeroelasticity, Scaling, Adaptive Structure, Efficiency, Nonlinear, Finite Element Analysis, N-MAS

16. SECURITY CLASSIFICATION OF:			**17. LIMITATION OF ABSTRACT**	**18. NUMBER OF PAGES**	**19a. NAME OF RESPONSIBLE PERSON**
REPORT	**ABSTRACT**	**c. THIS PAGE**			Dr. Robert Canfield (AFIT/ENY)
U	**U**	**U**	**UU**	111	**19b. TELEPHONE NUMBER** *(Include area code)* (937) 255-3636, ext 4723; e-mail: Robert.Canfield@afit.edu